A MICROSCOPIC ELECTRICAL IMPEDANCE SENSOR ARRAY FOR PRECISE TISSUE DELINEATION

A Master's Thesis

Presented to

The Faculty of the Division of Graduate Studies

By

Choongsoon Kim

Advisor Dr. Hua Wang

In Partial Fulfillment

Of the Requirements for the Degree

Master of Science in the

School of Electrical and Computer Engineering

Georgia Institute of Technology

May 2014

Copyright© 2014 by Choongsoon Kim

A MICROSCOPIC ELECTRICAL IMPEDANCE SENSOR ARRAY FOR PRECISE TISSUE DELINEATION

Approved by:

Professor. Hua Wang, Advisor
School of Electrical and Computer Engineering
Georgia Institute of Technology

Professor. Omer T Inan
School of Electrical and Computer Engineering
Georgia Institute of Technology

Professor. Jennifer O Hasler
School of Electrical and Computer Engineering
Georgia Institute of Technology

Date Approved: 20 March 2014

ACKNOWLEDGEMENTS

I would like to thank Dr. Hua Wang for giving me this great opportunity to join his research group (GEDC) and help me to engage in scientific study. This is definitely a valuable experience in my life and it has greatly extended my knowledge. Thank you for your guidance and support through the entire research process. This work would not have been possible without your help and support. I also thank our collaborator Prof. Jie Zhang at the University of Kentucky for his guidance and support. I would also like to thank the thesis committee members, Dr. Hasler and Dr. Omer Inan, for spending valuable time during my thesis process and giving me insightful recommendations.

I also would like to thank all of my lab members and other people that supported and encouraged me to finish my work. I greatly appreciate Chengjie (Bert) Zhu's positive attitude during the entire project period and the programming skills. As an undergraduate research assistant, he did a great job and I can definitely say that I was not able to finish the project without him. I also want to thank JongSeok Park for his knowledge and technical guidance whenever I was faced the obstacles. I also thank Song Hu for helping me with my system implementation and setting up the laboratory system. I could have not been able to pass through all that work without him. I am also appreciative of Chi Taiyuan for his technical support regarding circuit analysis. I also like to thank Michael Kroger for his teaching me about the Linux system, programming, and also providing me with his hands on experience in the lab during my studies.

Last but not least, I would greatly like to thank all of my family. Although we have not been in the same place, they have supported and encouraged me throughout my entire study abroad mentally, physically and financially in every aspect of my life. I thank my father for his valuable lessons and comments and also for praying for me. Whenever I have a talk with him, it has been really encouraging and inspiring. He is definitely my role model in my life and I really thank him for everything. I also thank my mother for being in good shape without me and I thank her for her encouragement and prayer. She made me so comfortable and relaxed whenever I was faced with a problem. She brought my motivation back to focus to my study. I also thank my sister and her family for all their support and encouragement through my entire study. Most importantly, I thank God for His mercy, righteous, and faithfulness. He has given me vision, purpose and meaning for my life.

TABLE OF CONTENTS

Page

ACKNOWLEDGEMENTS iii

LIST OF TABLES vii

LIST OF FIGURES viii

SUMMARY xi

CHAPTER

CHAPTER 1: Introduction 1

1.1 Motivation 1

1.2 Background 2

1.3 Organization 3

CHAPTER 2: Biological Tissue Impedance and Measurement Methodology 5

2.1 Electrical Properties and Frequency Dependency of Tissues 5

2.1.1 Conductivity and Permittivity 5

2.1.2 Electrical Circuit Analysis of Tissues 7

2.2 Tetrapolar Impedance Measurement Method 9

2.2.1 Electrode Array Modeling and Scanning Mechanism 10

2.2.2 Verification of Deep Tissue Penetration 14

2.3 Efficient Finite Element Simulation with Z-Parameter Matrix 17

CHAPTER 3: Finite Element Model Simulation and Verifications 21

3.1 2D Demonstration 21

3.2 3D Demonstrations and Impedance Mapping Image Results 24

3.3 Demonstration based on a 3D MRI Derived Brain Model 37

CHAPTER 4: PCB Implementation of an Electrical Impedance Sensor Array 43

4.1 Impedance Sensor Array Circuit 43

4.1.1 System Level Overview 43

4.1.2 Current Sourcing Circuit 44

4.1.3 Voltage Measurement Circuit 52

4.2 Automated Measurement Multiplexer System 56

CHAPTER 5: Measurement Setup and Measurement Results 59

5.1 Measurement Setup 59

5.2 Measurement Results 64

5.3 Discussion 76

CHAPTER 6: Summary and Conclusion 78

APPENDIX A: Performance of the modified Howland circuit 79

REFERENCES 81

LIST OF TABLES

Page

Table 1: Design Parameter of Healthy and Cancer Regions 21

LIST OF FIGURES

Page

Figure 2.1: Electrical circuit interpretation of a biological cell…….…….…….8

Figure 2.2: Biopolar and Tetropolar impedance measurement method description with current conduction path……..….9

Figure 2.3: A large-scale electrode array model with dielectric substrate…….11

Figure 2.4: Graphical interpretation of horizontal and vertical scanning methods for impedance mapping image…….....12

Figure 2.5: Proposed various electrode configurations……..13

Figure 2.6: Large electrode separation and the possible current conduction path for deep tissue penetration……...14

Figure 2.7: Deep tissue verification model generated in COMSOL Multiphysics® with different configuration……...……15

Figure 2.8: Simulation result of deep tissue penetration……..….….16

Figure 3.1: A simple geometry for artificial normal brain and tumor tissue regions……22

Figure 3.2: Tetrapolar impedance measurement model…….……23

Figure 3.3: Simulation result of impedance variation at the boundary for each frequency…….…..23

Figure 3.4: 10 ×10 electrode array model in COMSOL Multiphysics®…….……..25

Figure 3.5: Cylindrical and L-shaped tumor boundary used to verify the impedance mapping image algorithm……..25

Figure 3.6: Simulation model and corresponding impedance mapping image in horizontal and vertical scan……26

Figure 3.7: Graphical interpretation of the method of combining impedance data for horizontal and vertical scan…….……..27

Figure 3.8: The combined impedance mapping image of the different tissue boundaries detected by the electrode array……..28

Figure 3.9: Impedance mapping image of L-shaped boundary measured from 200um distance……..30

Figure 3.10: Impedance mapping image of Cylindrical-shaped boundary measured from 200um distance……..31

Figure 3.11: Impedance mapping image of L-shaped boundary measured from 300um distance……..32

Figure 3.12: Impedance mapping image of Cylindrical-shaped boundary measured from 300um distance……..33

Figure 3.13: Impedance mapping image of L-shaped boundary measured from 400um distance……..34

Figure 3.14: Impedance mapping image of Cylindrical-shaped boundary measured from 400um distance……..35

Figure 3.15: The sequence of the finite element model image process by SIMPLEWARE(LTD., UK)……..38

Figure 3.16: (a) Simulation setup of tumor and the electrode array at the boundary. (b) 20×20 Electrode array with 100 terminal sparsely selected……..39

Figure 3.17: Impedance mapping image of MIR derived brain model measured from 100um and 200um distance ……..41

Figure 3.18: Impedance mapping image of MIR derived brain model measured from 300um and 400um distance ……..42

Figure 4.1: Automated electrode array impedance measurement system……..43

Figure 4.2: A simple current source model with load impedance Z_L and the output impedance Z_s presented…….…….……..45

Figure 4.3: Schematic of a modified Howland current sourcing circuit using both positive and negative feedback…….……..46

Figure 4.4: Schematic of single ended input to differential output generator circuit…....48

Figure 4.5: The full schematic of the differential modified Howland circuit……...49

Figure 4.6: OrCAD Capture simulation schematic of the differential modified Howland Circuit.....50

Figure 4.7: The differential modified Howland circuit simulation results. (a) AC simulation, (b) Transient simulation…….51

Figure 4.8: Schematic of the instrumentation amplifier……....52

Figure 4.9: OrCAD Capture simulation schematic of the instrumentation amplifier…….....54

Figure 4.10: AC simulation result for the instrument amplifier (frequency vs dB)……..54

Figure 4.11: Transient simulation result of the instrumentation amplifier……55

Figure 4.12: ADG1406 pin configuration and the corresponding truth table……56

Figure 4.13: Multiplexer configurations for horizontal and vertical scanning mechanism…….57

Figure 5.1: Printed circuit board manufactured by Advanced Circuit…….....59

Figure 5.2: Fully constructed voltage and current circuits……60

Figure 5.3: Multiplexer system and the circuits soldered on a separated board; only four current and voltage path are connected.....62

Figure 5.4: Complete PCB impedance sensor system with petri dish attached for tissue measurements……63

Figure 5.5: Experimental setup for electrode array impedance sensor system for different tissue boundary detection……..64

Figure 5.6: Measurement direction on the electrode array and muscle fiber direction indicated by yellow arrow…….68

Figure 5.7: Measurement setup and impedance mapping image of fat and muscle tissues……70

Figure 5.8: Measurement setup and impedance mapping image of two different layers...…….…….....71

Figure 5.9: Measurement setup and impedance mapping image of muscle-fat-muscle three layer case……..72

Figure 5.10: Measurement setup and impedance mapping image of the pile of tissues; fat layer at the bottom and mixed fat-muscle layer at the top……73

Figure 5.11: Measurement setup and impedance mapping image of the pile of tissues; fat layer at the bottom and half side fat at the top……..74

Figure 5.12: Measurement setup and impedance mapping image of testing impedance variation based on anisotropic property of the tissue……75

SUMMARY

Bioelectrical impedance measurement is a widely used technique to estimate the composition of the human body and it also has many medical sensing applications. The tetrapolar impedance measurement method is a credible impedance measurement technique for bioelectrical impedance applications. The tetrapolar measurement method can be repeatedly performed on a large scaled electrode array, which is massively-parallel and highly scalable and it enables the impedance mapping image technique. The electrical impedance sensing array is capable of delineating different tissue boundaries by highly reconfigurable electrode selections. COMSOL Multiphysics® simulation has been performed to verify this concept. Two-dimensional impedance mapping data of the tissue boundary has been acquired and plotted onto a user-friendly colorful image. For a more realistic simulation, a Magnetic Resonance Imaging (MRI) derived finite element brain/tumor model has been generated. The electrode system was then combined with MRI models and a tumor boundary has been generated by the impedance mapping image. As the last step, a Printed Circuit Board (PCB) system was implemented for proof-of-concept experimental verification.

CHAPTER 1

INTRODUCTION

1.1 Motivation

Bioelectrical impedance has been used in medical field for diagnosis, characterizations of body composition and sensing purposes. Many impedance sensing techniques have been developed and used in various other applications. Real time guidance surgery, electrical impedance tomography (EIT), cell based impedance biosensor and electrochemical impedance sensor. Estimating body composition is a typical application of bioelectrical impedance analysis. Casas et al. (1996) designed the impedance measurement system using an array of 16 electrodes to monitor cardiac-related events. Also, Cherepenin et al. (2002) proposed an electrode array system consisting of 256 electrodes that can enable the imaging of breast tissues. In addition to that, Tidswell et al. (2001) used scalp electrode systems to investigate human brain activity by analyzing impedance changes. Moreover, electrical the impedance sensing method has been used for ischemia detection (Yúfera et al., 2005), as a real-time impedance sensing biopsy needle (Mishra et al., 2012), and detection of multiphase flow phenomena in chemical vessels and pipelines (Wang et al., 2002).

Among the various applications, this thesis mainly focuses on precise different tissue boundary delineation based on their different impedance property. The sensing technique and the verification model are applied for tumor boundary detection during the minimally invasive surgery.

The major challenge of tumor surgery is to remove tumors while preserving as much of the healthy tissue as possible. Most of the tumors can be removed through surgical procedures, but there are tumors that are often left behind after the surgery and this can possibly cause cancer reoccurrence. Precise boundary delineation of the tumor and the healthy tissue is very difficult to detect with bare eyes even for an experienced surgeon. To address this challenge, there is a tremendous need for high performance image sensing techniques which can clearly delineate the tumor boundary and also enable real time guidance surgery. Unfortunately, there are no current medical imaging techniques that satisfy those capabilities.

To bridge this unmet gap between market and technology, novel sensing technology has been proposed to enable accurate and specific delineation of the different tissue boundaries. The proposed technique is based on the bioelectrical impedance analysis (BIA) which has the capability to produce a 2D impedance mapping image of different tissue boundaries. The main focus of the system is the impedance measurement electrode array that is capable of precise tumor and healthy tissue boundary delineation which is dependent on different dielectric properties.

1.2 Background

BIA is a common non-invasive method of detecting different body compositions and tissue characterizations based on different electrical properties (Ogunnika et al., 2010). The method is simple. An alternating electrical current is sent through the body and the system measures the resistivity of the current flow when it passes through the different parts of

body. The body consists of many types of conducting material such as water, blood, bone, tissues, and so on. Materials such as water and blood have high conductivity for which the current flow would not be as resistive as bone and fat, which have low conductivity. These electrical properties have been used for tissue-level diagnostics for a long time (Zhang and Patterson, 2010). Much of the literature has reported on various tissue impedances and their corresponding electrical properties such as conductivity and permittivity (Gabriel et al., 1996).

The tetrapolar measurement method has been used for bioelectrical impedance measurement purposes. This measurement method is normally used to create an image of the body composition and Robillard and Poussart (1979) investigated the spatial resolution of impedance measurement using the tetrapolar measurement method. In addition, the tetrapolar measurement method is often used in EIT (Electrical Impedance Tomography) to compute the electrical conductivity and permittivity distribution in an object (Saulnier et al., 2001).

1.3 Organization

The goal of this thesis is to verify the initial concept of the impedance mapping of the tissue boundary and to implement a PCB level design. The concept behind the impedance mapping image is verified by COMSOL Multiphysics®. Also, a PCB level system has been implemented and the impedance imaging of tissues (muscle and fat) has been performed. All of the procedures and steps are organized in the following chapters listed below.

Chapter 2.1 explains the basic electrical properties of biological tissues and their frequency dependencies. In addition, the tetrapolar measurement method is introduced as an impedance measurement technique and the extended electrode array is proposed to enable an impedance mapping image. The efficient finite element simulation using a Z-parameter matrix is also discussed.

Chapter 3 demonstrates a 3D finite element model simulation in COMSOL Multiphysics®. Simple cylindrical and L shaped boundary shape detection and MRI derived brain/tumor model are used for the verification of the impedance mapping image simulation and the deep tissue penetration method is verified with different electrode configurations.

Chapter 4 presents the detailed design of the PCB electrode impedance array system with the current sourcing and voltage measurement circuits. Multiplexers are used to enable the automatic measurement system and binary addresses are controlled by NI LabView.

Chapter 5 discusses the measurement setup, results, and discussion.

Chapter 6 covers the summary and the future work.

CHAPTER 2

BIOLOGICAL TISSUE IMPEDANCE AND MEASUREMENT METHODOLOGY

2.1 Electrical Properties and Frequency Dependence of Tissues

2.1.1 Conductivity and Permittivity

Biological tissues have their own frequency dependent electrical properties such as conductivity and permittivity. After Oliver Heaviside discovered the concept of electrical impedance, it has attracted many scientists' attention for a long time. Conductivity and permittivity are well known electrical properties which determine the path of electrical current flow through biological tissues. Conductivity is a property that defines how well electric charges can pass through a material. Conductivity can be defined as a ratio of current density to the electric field shown below.

$$\sigma = \frac{E}{J} \tag{2.1}$$

Permittivity defines how well the electric field can be generated in a material and it is directly related to the susceptibility which defines the dielectric polarization of materials. The relation of polarization and susceptibility can be explained as below,

$$P = \epsilon_0 \chi_e E \tag{2.2}$$

where χ_e represents the susceptibility. Also the electric field density and electric field can be expressed in terms of susceptibility and permittivity.

$$\mathrm{D} = \epsilon_0(1 + \chi_e) \tag{2.3}$$

$$E = \epsilon_0\epsilon_r E = \epsilon E \tag{2.4}$$

The basic structure of biological cells consists of intra/extra cellular space with fluid, and the capacitance of the membrane (Smith 2008). The extra-cellular fluid is purely resistive and cell membranes are also highly resistive and capacitive (Pethig 1984). Thus, electric conductivity and permittivity are significantly related to tissue impedances. When the ideal capacitor is considered, the capacitance and conductance can be described as

$$C = \frac{\epsilon_0\epsilon_r A}{d} \tag{2.5}$$

$$G = \frac{\sigma A}{d} \tag{2.6}$$

where A is the area of the capacitor plate and d is the distance between the plates. The admittance of the capacitor can be expressed as

$$Y = (G + j\omega C) = (\sigma + j\omega\epsilon\epsilon_0)\frac{A}{d} \tag{2.7}$$

$$\mathrm{C} = \frac{Y}{j\omega} = \left(\frac{-j\sigma}{\omega} + \epsilon_0\epsilon_r\right)\frac{A}{d} \tag{2.8}$$

where

$$\epsilon = \epsilon' - j\epsilon'' \tag{2.9}$$

is the complex permittivity of the material and the imaginary part of ϵ is considered as loss. In equation (2.7), the $j\omega\epsilon\epsilon_0$ term can be negligible at low frequencies compared to the conductivity, which means that the impedance is more affected by conductivity at low frequencies.

On the other hand, the permittivity term becomes dominant as the frequency goes high. In a wide frequency range, the tissues show different changes and this frequency dependency is known as dispersion. In different frequency ranges, $\alpha, \beta,$ and γ dispersion regions exist (Foster, 2000). α-dispersion occurs at low frequencies (kHz) where the conductivity of the tissue is dominant. The α-dispersion is mainly affected by the extra-cellular fluid (Smith, 2008).

In the beta dispersion region (kHz to MHz), the electrical signal starts passing through the cell membrane. Since the electric current at this frequency can pass through the intra/extra cellular membrane, the cell membrane acts like a capacitor, which contributes to reactance of the impedance.

After beta dispersion, gamma dispersion occurs at the frequency range above 1 GHz. Most bioelectrical impedance applications focus on α- and β- dispersions since most changes between normal and malignant tissues occur in these frequency regions (Smith, 2008). In addition, electromagnetic wave interactions with the cellular structure of biological tissues are mainly detected in the α- and β- dispersion regions (Bertemes-Filho, 2002). Thus, this thesis focuses on the frequency region where α- and β- dispersion occurs.

2.1.2 Electrical Circuit Analysis of Tissues

Based on the information of cell structure and the capacitive characteristic of the cell membrane, the cell structure can be interpreted as a simple RC circuit as shown in Figure 2.1.

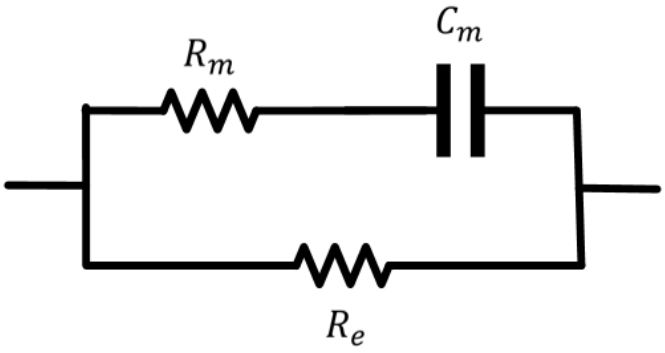

Figure 2.1: Electrical circuit interpretation of a biological cell (Frike and Morse, 1925)

The impedance of a simple RC circuit as shown in Figure 2.1 can be described as

$$R_{tot} = (R_m + \frac{1}{j\omega C_m}) \parallel R_e \tag{2.10}$$

At low frequencies, the capacitor behaves like an open circuit, so the total impedance is purely resistive which represents the external fluid resistance R_e. As the frequency goes high, the electrical current starts penetrating the cell membrane and the reactance of the tissue impedance starts to become considerable.

Different types of tissues have their own dielectric properties. Specifically, malignant tissues have higher conductivity and permittivity than healthy tissues because of their increased nuclear size, enlarged nucleoli, and irregular chromatin distribution (Smith, 2008). A tumor is a malign tissue that can grow faster than normal and scientists have discovered that malign tissues have higher conductivity and permittivity than normal tissues (Gabriel et al., 1996). Therefore, the tumor tissue exhibits lower impedance than healthy tissues.

2.2 Tetrapolar Impedance Measurement Method

There have been various bioelectrical impedance measurement techniques but the tetrapolar measurement method is the most widely used method in various fields such as geophysics, microelectronics, and also to characterize myocardial tissue (Binette et al., 2004). Compared to the bipolar measurement method, the tetrapolar measurement method uses four electrodes. The difference is that tetrapolar measurement method has separate current injection electrodes and voltage measurement electrodes. For the bipolar measurement method shown in Figure 2.2 (a), only two electrodes are used, and the injected current and measured voltage use the same pair of electrodes.

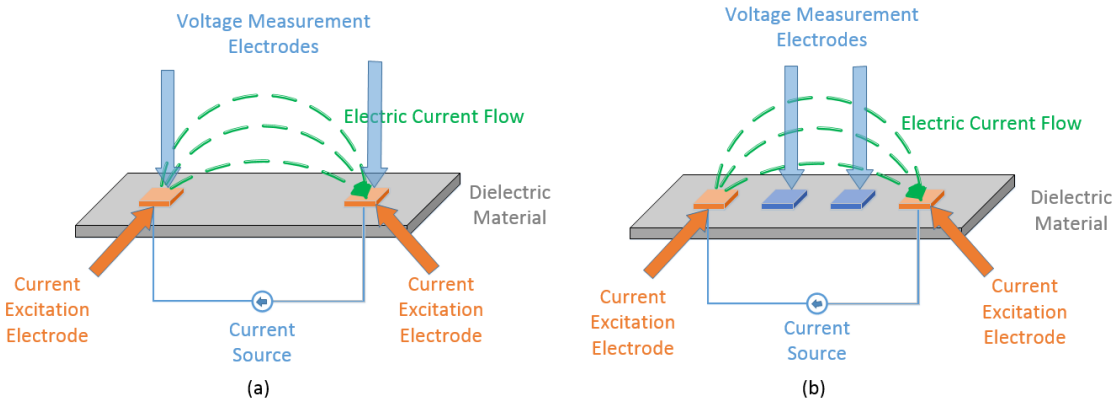

Figure 2.2: Bipolar and tetrapolar impedance measurement method description with current conduction path

As shown in Figure 2.2 (b), the current is injected through the outer pair of electrodes as shown by the orange arrows. The electric field due to the current causes a potential voltage between the inner electrodes. From the potential voltage and known injected current, the impedance of specific tissues can be determined.

Since the bipolar measurement method shares the same current and voltage electrode pair, there is an additional voltage drop induced from the polarization at the electrode surface which is added to the voltage measured from the tissue alone. This polarization effect makes the impedance analysis less accurate because this additional voltage drop would make it difficult to find the actual tissue impedance due to the added contact impedance (Binette et al., 2004). The tetrapolar measurement method can reduce this electrode polarization problem by adding two different electrodes for voltage measurements. Typically, a current source has a high output impedance to inject the current forcefully into the tissues. Also, the voltage measurement equipment has a high input impedance. Because of the high impedance of the voltage measurement amplifier, the contact impedance from the electrodes is relatively negligible. Therefore, the tetrapolar measurement method can measure more accurate impedance when the electrodes are attached to biological tissue.

2.2.1 Electrode Array Model and Scanning Mechanism

Instead of the single impedance value, a spatial resolution of the impedance measurement can be implemented by extending four electrode measurements to a large-scale electrode array. Figure 2.3 shows the model of the electrode array.

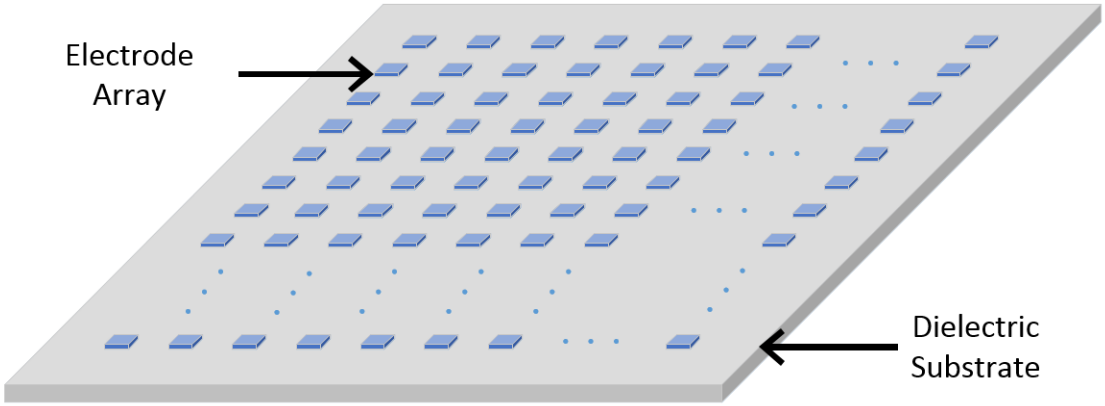

Figure 2.3: A large-scale electrode array model with dielectric substrate. The electrode array can optimize the spatial resolution, sensitivity and enables the impedance mapping system by repeating tetrapolar impedance measurements

By repeating the tetrapolar measurement method over the entire array, 2-dimensional impedance data over the tissue surface can be obtained and further reconstructed into a user-friendly impedance mapping image. The array method has a lot of advantages in that it optimizes spatial resolution, sensitivity, and high reconfigurability of electrodes.

The large scaled electrode array enables spatial level impedance mapping with high resolution. The tetrapolar measurement method states that only one set of four electrodes are in use at any given time. The meaning of scanning is simply repeating tetrapolar measurements with a different electrode set over the entire electrode array. The set can be chosen with any configuration in any location on the array. The accumulated impedance data from various electrode sets can be reconstructed to a 2D impedance mapping image which provides clear tissue boundary detection. The detailed scanning methodology is presented in Figure 2.4 with a basic four consecutive electrode configuration. The set is chosen in both horizontal and vertical directions and each set moves one by one in each direction.

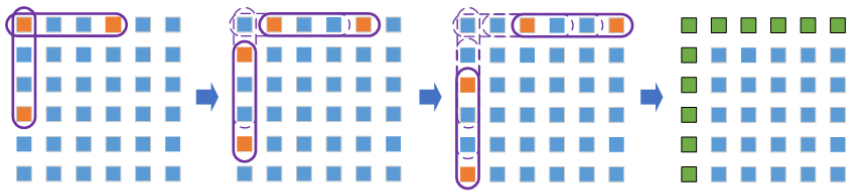

(a) Scanning of First Row and Column

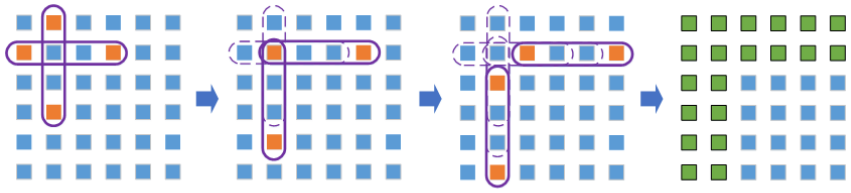

(b) Scanning of Second row and Column

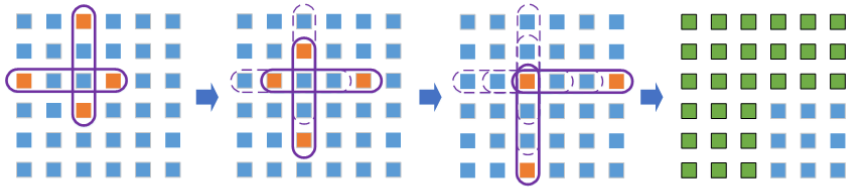

(c) Scanning of Third Row and Column

Figure 2.4: Graphical interpretation of horizontal and vertical scanning methods for impedance mapping image. Basic set of four electrodes continuously moves one by one in each direction and it results in scanning the specific area where the electrode array covers

As shown in Figure 2.4, the current is injected into the outer electrode pair and the voltage is measured from the inner electrode pair. The impedance data is independently stored whenever the electrode set changes the location. In Figure 2.4 (a), the first row and column is continuously scanned and the green electrodes in the right-most image indicate the areas where the impedance values were measured. Figure 2.4 (b) and (c) show the scan of the second and third row/column measurements executed in the same manner as before.

Instead of choosing four consecutive electrodes, various electrode configurations are possible for an electrode array. The various electrode configurations are shown in Figure 2.5.

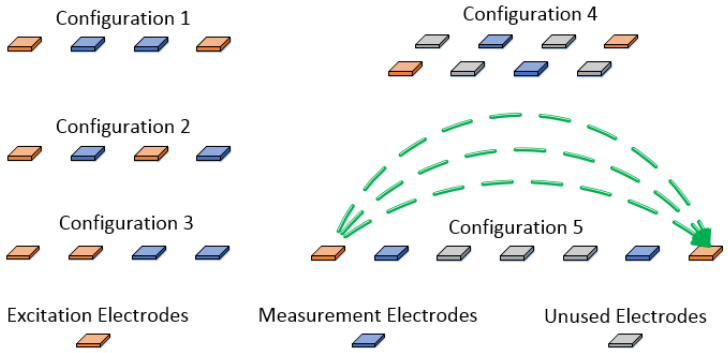

Figure 2.5: Proposed various electrode configurations: Consecutive four linear electrode selections, configuration 1 ("1-4-2-3" selection), excites the first and forth electrodes as current source (red) and the second and third electrodes as voltage measurement ports

As Figure 2.5 shows, there are many possible configurations available using one and two dimensional electrode selections. The Configuration 1 is from now on denoted as notation "1-4-2-3" for simplicity. The number simply indicates the order of the electrodes. "1-4" represents the current injecting electrodes and "2-3" indicates the order of the voltage measurement electrodes. Likewise, Configuration 5 is denoted by "1-7-1-6" notation. Configuration 5 depicts the largely separated current injection electrodes and shows possible current conduction paths through a medium. This configuration assumes the current would conduct a further distance, which can be useful for deep tissue penetration. Selecting random electrodes in the system allows flexibility for surgeons in tumor removal procedures while minimizing possible damage to healthy tissues during surgery.

2.2.2 Verification of Deep Tissue Penetration

As described in Figure 2.6, large electrode selections would make possible deep tissue detection. Compared to the basic four consecutive electrode configurations, if the distance of the current electrodes is larger, the current conduction area becomes larger. Figure 2.6 shows possible changes in the current flow when the different current electrodes are selected.

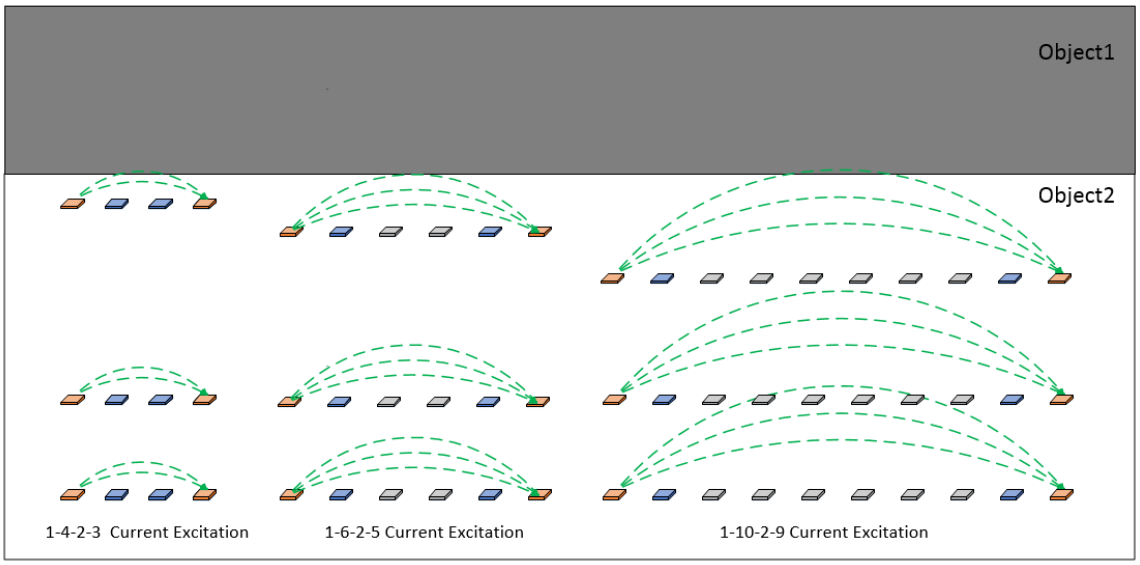

Figure 2.6: Large electrode separation and the possible current conduction path for deep tissue penetration, which can detect the boundary from a further distance

As shown in Figure 2.6, as the distance between each current injecting electrode increases, the area of current conduction also increases. For the 1-4-2-3 configurations, the electrode may need to get closer to Object 1 to detect the boundary. However, the 1-10-2-9 configurations can detect the boundary from a further distance because the current conduction propagates to a larger distance than the 1-4-2-3 configurations. The verification model and the four types of different configurations are shown in Figure 2.7. Configuration 1 is the basic consecutive four electrode selection. The electrode selections of the other

configurations are shown in Figure 2.7. The table shows the center to center distance between voltage measurement electrodes.

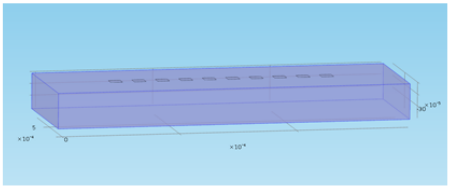

- Electrode Size : 100um

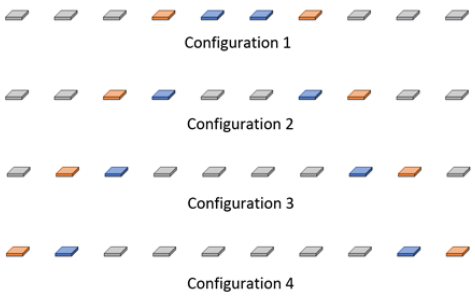

Table. Distance between voltage electrodes

	Distance
Configuration 1	200 um
Configuration 2	600 um
Configuration 3	1000 um
Configuration 4	1400 um

Figure 2.7: Deep tissue verification model generated in COMSOL Multiphysics® with different configurations

The verification method is simple. The same simulation environment was set and the electrode model was located near the boundary of the two regions. The impedance is measured by each configuration and the electrode moves away from the boundary. As the distance increases, there is a threshold distance where the impedance value is stabilized and the electrode can no longer detect the boundaries. Based on the different threshold distances for each configuration, the possibility of deep tissue penetration can be verified. The results are shown in the graph of Figure 2.8. As Figure 2.8 shows, the x-axis indicates the distance from the boundary to the electrode array and the y-axis is the percent difference between the stabilized impedance value and the impedance at each distance.

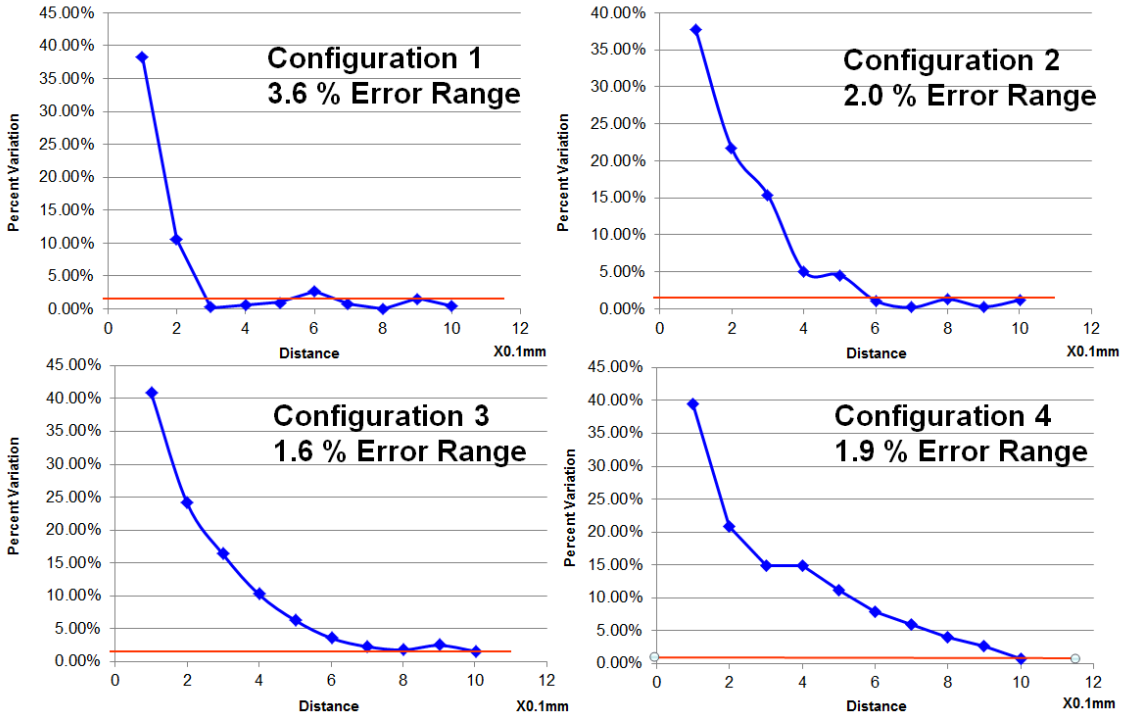

Figure 2.8: Simulation results of deep tissue penetration

The error range in each graph indicates the possible range of impedance variation caused by the simulation error inside the same material. Therefore, if the percentage difference between the stabilized impedance and the measured impedance value is larger than the error range, then the impedance variation is caused by different tissue detection. The stabilized value was calculated over a 6σ range of sample impedance data measured from a distance where it is far enough such that the electrode array does not detect the boundary impedance. For example, the error range is 3.6% for Configuration 1 and the percentage difference becomes less than 3.6% after a distance of 0.3mm, which means that the threshold distance is 0.3mm for this configuration. As the separation between electrodes increases, the threshold distance keeps increasing. The threshold distance of Configuration 2 is 0.5mm and Configuration 3 is about 0.7~0.8mm. Lastly, Configuration 4 (1-10-2-9)

shows a 1mm threshold distance, which is three times larger than Configuration 1. As the area of the current conduction increases, the impedance value is also increased. An important aspect regarding the impedance data analysis here is that it should be dependent on the relative variation of the impedance for each configuration, not the absolute impedance data comparison between all configurations.

2.3 Efficient Finite Element Model Simulation with Z-Parameter Matrix

To verify the impedance mapping of different tissue boundaries, the tetrapolar measurement method has to be repeated through the entire electrode array with various configurations. In the case of a large scaled N × N electrode array, it is a tedious job to reassign current and voltage terminals every time when different electrode sets are selected. To facilitate the scanning mechanism and impedance evaluation, microwave networks and a Z-Parameter matrix are applied to the impedance mapping system. In the case of an arbitrary N-port microwave network, each port introduces incident and reflected current and voltage. Each electrode can be defined as a port, so that the current/voltage relationship can be described with following the impedance Z-matrix form (Pozar 2002)

$$\begin{bmatrix} V_1 \\ V_2 \\ \vdots \\ V_N \end{bmatrix} = \begin{bmatrix} Z_{11} & \cdots & Z_{1N} \\ Z_{21} & \cdots & Z_{2N} \\ \vdots & \cdots & \vdots \\ Z_{N1} & \cdots & Z_{NN} \end{bmatrix} \begin{bmatrix} I_1 \\ I_2 \\ \vdots \\ I_N \end{bmatrix} \tag{2.11}$$

From the matrix description above, the impedance value is obtained from the Equation 2.12 below

$$Z_{ij} = \left.\frac{V_i}{I_j}\right|_{I_k=0\ for\ k\neq j} \tag{2.12}$$

Equation 2.12 indicates that the impedance, Z_{ij}, is obtained when the current is injected into port j and the open-circuit voltage is measured from port i while opening all other ports ($I_k = 0\ for\ k \neq j$). If the indices of the current ports are i and j, and voltage ports are p and q respectively, a basic Z-matrix can be represented as following

$$\begin{bmatrix} V_1 \\ V_p \\ V_q \\ \vdots \\ V_N \end{bmatrix} = \begin{bmatrix} Z_{11} & \cdots & Z_{1N} \\ Z_{p1} & \cdots & Z_{2N} \\ Z_{q1} & \cdots & Z_{qN} \\ \vdots & \cdots & \vdots \\ Z_{N1} & \cdots & Z_{NN} \end{bmatrix} \begin{bmatrix} 0 \\ I_i \\ -I_j \\ \vdots \\ 0 \end{bmatrix} \tag{2.13}$$

The matrix form indicates that the N-port network can produce an N×N Z-matrix by sweeping entire ports based on the impedance calculation in Equation 2.12. Positive current I_j is injected into port i and negative current -I_j is coming out from port j. Thus the voltages at port p and q are simply determined by

$$V_p = Z_{pi}I_i - Z_{pj}I_j \tag{2.14}$$

$$V_q = Z_{qi}I_i - Z_{qj}I_j \tag{2.15}$$

To find the potential difference between ports p and q, Equations 2.14 and 2.15 are subtracted

$$V_p - V_q = Z_{pi}I_i - Z_{pj}I_j - (Z_{qi}I_i - Z_{qj}I_j) \tag{2.16}$$

$$I_i = I_j = I \tag{2.17}$$

Based on the basic Ohm's law, the final impedance Z can be calculated as

$$\frac{V_p - V_q}{I} = Z_{pi} - Z_{pj} - (Z_{qi} - Z_{qj}) \tag{2.18}$$

$$Z_{pq/ij} = Z_{pi} - Z_{pj} - Z_{qi} + Z_{qj} \tag{2.19}$$

The Z-parameter matrix of the network produces impedance data of every combination of current and voltage electrodes. The final Equation 2.19 means that as long as the indices of the current ports and voltage ports are known, the impedance value of the selected four electrodes on the array can be found from the original Z-parameter matrix. COMSOL Multiphysics® has a built in parametric simulation that can evaluate the Z-matrix of all ports assigned as terminals. The parametric simulation evaluates the impedance of all possible combinations of electrode ports, and it produces a Z-matrix. For example, consider a 10 × 10 electrode array. In this case, 100 electrodes are available for tetrapolar measurement method. This 10 × 10 electrode array produces a 100 × 100 impedance matrix, a total of 10,000 impedance values. Those 10,000 impedance values can be reconstructed through the Equation 2.19 with proper electrode selections. The impedance value of any electrode configuration can be obtained by plugging in the index of current and voltage electrode ports into Equation 2.19. The final meaningful impedance value is the combination of four impedance values selected from the original Z-matrix data. This equation and the parametric sweep data together would facilitate the impedance mapping

system verification and enable reconfigurable scanning capabilities of the electrode array. Scanning with various configurations as shown in the previous chapter can be easily performed using only the indices of the current and voltage electrodes.

CHAPTER 3

FINITE ELEMENT MODEL SIMULATION AND VERIFICATION

3.1 2D Demonstration

To verify the impedance variation of tissue based on their electrical properties, COMSOL Multiphysics® modeling and simulation was performed. AC/DC physics with a frequency domain electric current module has been chosen.

An artificial brain with tumor tissues was modeled using simple geometry. One rectangular box was created and separated into two regions, the tumor and the healthy tissue. Bioelectrical impedance is mainly performed in alpha and beta dispersion regions where conductivity and permittivity are the main factors that affect the impedance analysis. Since 77~78% of the brain composition is water, the water was assigned as the basic material of the two separated regions and then different conductivities and permittivities were assigned to each respective region. The conductivity of healthy brain tissue and the tumor region (Glioblastoma) was determined via MRI scans; the conductivity of white matter of the brain is 0.4 S/m and the Glioblastoma region is 1.02 S/m.

Table 1. Design parameter of healthy and cancer regions.

Frequency	Parameters	Healthy Regions	Cancer Region
1 MHz	Conductivity	0.4 [S/m]	1.02 [S/m]
	Permittivity	70	80
100 MHz	Conductivity	0.4 [S/m]	1.02 [S/m]
	Permittivity	70 – 2j	80 – 2j
1 GHz	Conductivity	0.4 [S/m]	1.02 [S/m]
	Permittivity	65 -3j	75 -4j
		Current Applied	0.1 mA

The measurement values were acquired from St Thomas Hospital in London (Voigt, 2001). Table 1 shows dielectric properties assigned to each region for different frequencies. Permittivity values of water at different frequencies were reported by (Chaplin, 2013). Figure 3.1 shows the simulated model in COMSOL Multiphysics®. The upper region is considered healthy brain tissue and the lower region is tumor tissue. The box size dimensions are 10mm $\times$ 10mm $\times$ 20m. A single electrode is 100um $\times$ 100um and the distance between the electrodes are also 100um. The four electrode model is initially placed inside the tumor region.

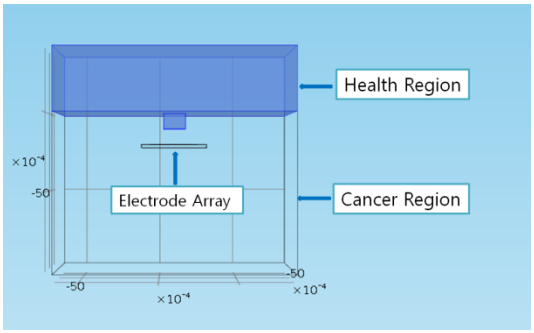

Figure 3.1: A simple geometry for artificial normal brain and tumor tissue regions

The first impedance measurement was performed when the electrode model was located far away from the boundary of the two regions. Then, the distance between the electrode and the boundary is continuously reduced while measuring the impedance at each position. The four electrode model is shown in Figure 3.2. Current conservation is applied to all three domains: the benign, the cancer regions, and the electrode array. Electrical insulation is applied to all boundaries except the domains that are in contact with the electrodes. The model is meshed in extra fine detail. Also, simulations were conducted with a tolerance factor of 1e-6. The simulation was performed at 1 MHz, 100 MHz, and 1 GHz to see how the impedance varied in different frequency ranges.

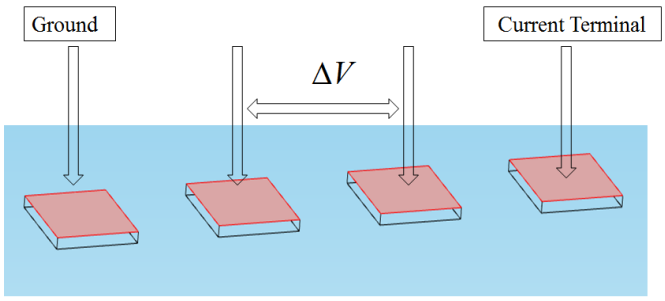

Figure 3.2: Tetrapolar impedance measurement model. AC current is generated from one of the current electrodes and the current flowing through the tissue goes into another electrode set as ground. Then, the potential voltage is measured between the two inner electrodes

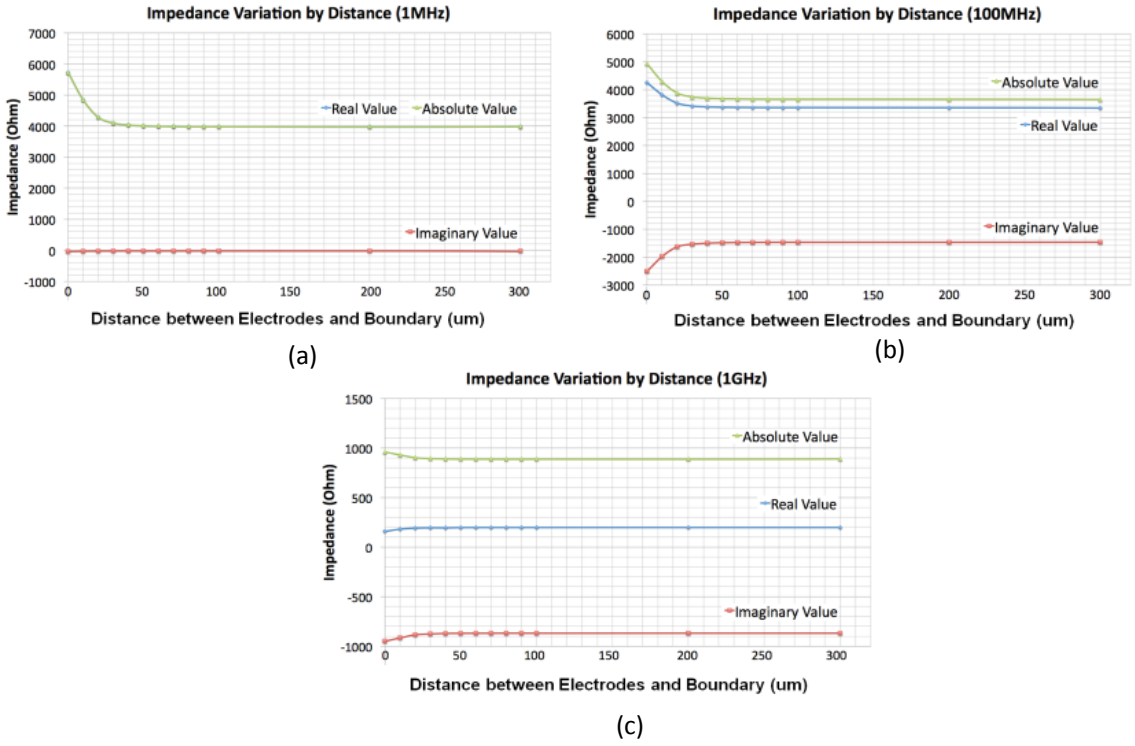

Figure 3.3: Simulation results of impedance variation at the boundary for each frequency. As the distance between the boundary and electrode is reduced, the impedance increases as shown on the graph.

Figure 3.3 shows the simulation results at each frequency. At each frequency, the impedance-distance graph shows the same behavior of the impedance increasing as the

distance between the electrode model and the boundary decreases. The green line indicates the absolute value of the impedance and the blue line represents the real part of the impedance (resistance). Lastly, the red line shows the imaginary part of the impedance value (reactance). In the 1 MHz graph, the absolute value is almost the same as the real impedance value and the imaginary part of the impedance is almost zero. As discussed before, it is now verified that the impedance is purely resistive at low frequencies. In the 100 MHz case, the situation is different. The imaginary part of the impedance starts increasing but it is not a dominant factor at this frequency. However, in the 1 GHz case the situation is completely changed. The real impedance value is reduced to almost zero and the reactance of the impedance dominates. Therefore, the absolute value of the impedance is similar in magnitude to the imaginary impedance value. This simple verification proves that any material that has different dielectric properties shows an impedance difference and it can be verified by the tetrapolar measurement method. In addition, depending on the frequency range, the impedance varies between being largely resistive and largely reactive.

3.2 3D Demonstration and Impedance Mapping Image Results

With the same simulation setup as in section 3.1, the large scaled electrode array model has been generated to produce a 2D impedance mapping image of the tumor boundary. Figure 3.4 shows the electrode array model generated in COMSOL multiphysics®.

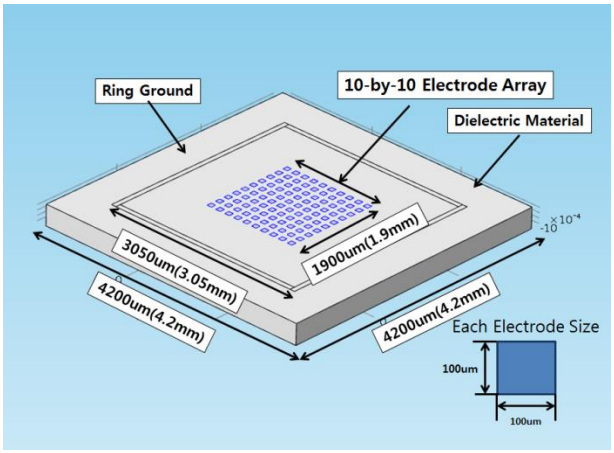

Figure 3.4: 10 ×10 Electrode array model in COMSOL Multiphysics®

The verification started with a 10 ×10 electrode array. The electrode array was created upon the silicon substrate and has a global ring ground around it. Each electrode size is 100um and the displacement between each electrode is 100um as well. The total length of the array is 1.9 mm. The distance between the electrode array and the ring ground was set at 500um to minimize the amount of current flowing into the ground. For this simulation, the tumor boundary was given a simple shape to verify that the electrode array can detect the shape of the boundary. Figure 3.5 shows the simple cylindrical and L-shaped boundary models.

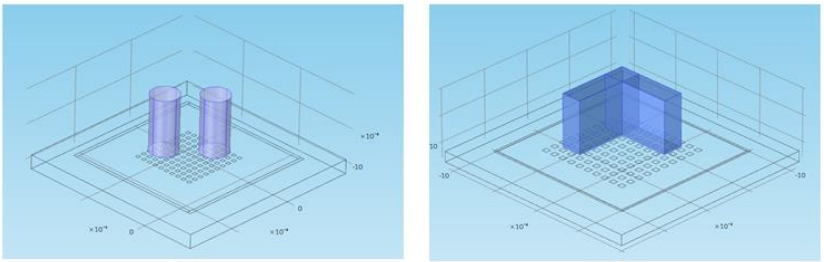

Figure 3.5: Cylindrical and L-shaped tumor boundary used to verify the impedance mapping image algorithm

As previously discussed, the Z-matrix simulation has been initially performed far away from the boundary. Then, the distance between electrode and the boundary gets closer until the electrode array detects the impedance variation. Every time the Z-matrix simulation is performed, the Z-matrix is reconstructed using Equation 2.19 while applying the scanning method in Figure 2.4. The reconstructing impedance data process and image plot has been done using Matlab. The resulting impedance values indicate the average impedance of certain areas where the electrode sets are located. After reevaluating the impedance data after scanning the 1-4-2-3 configuration, the reconstructed Z-matrices are produced; 10 × 7 (row × column, horizontal scan) and 7 × 10 (row × column, vertical scan) for a 10 × 10 electrode array. The reconstructed Z-matrices in horizontal and vertical scanning are plotted onto the impedance mapping images as shown below in Figure 3.6.

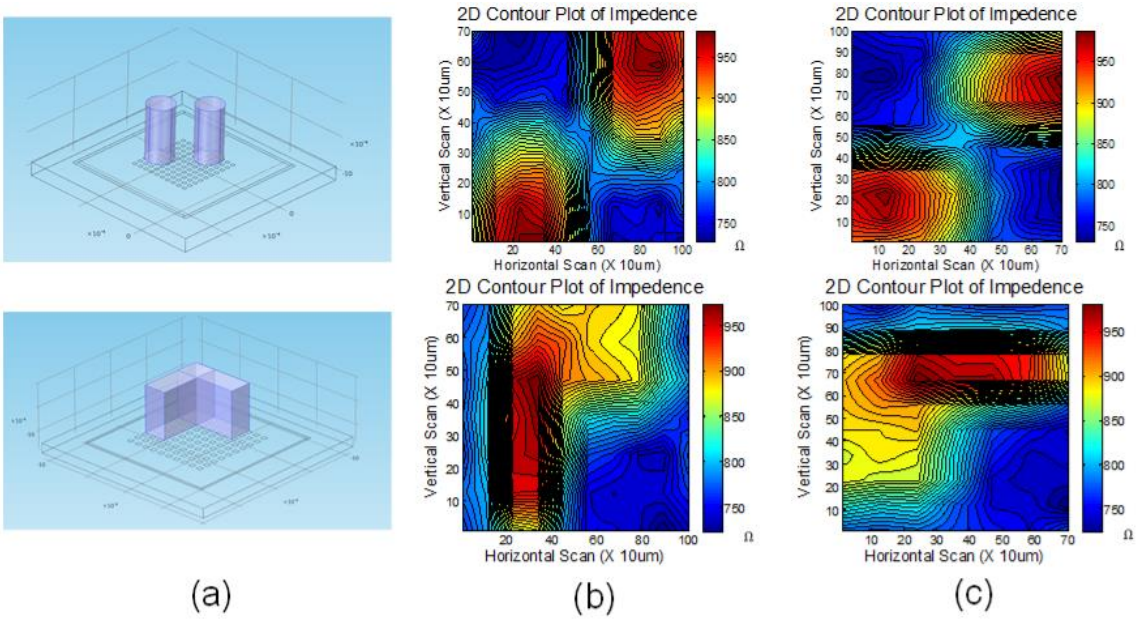

Figure 3.6: Simulation model and corresponding impedance mapping image in horizontal and vertical scan; (b) vertical scan image, (c) horizontal scan image

Since the electrode array has a size of 10 × 10, there is a small sample size of impedance data available for the image plot. Therefore, the data is interpolated between impedance data points to increase the resolution of the impedance mapping image shown in Figure 3.6. Figure 3.6 (b) shows the impedance mapping image derived from the vertical scan and (c) shows this image for the horizontal scan. As shown in the images, the boundary shape is vertically and horizontally spread, which does not show the accurate boundary shape. This is possibly caused by some missing impedance data for a specific area between each row and column and electrode corners. In order to compensate for the missing impedance data of certain physical areas due to the one-directional scan, horizontal and vertical matrices are combined to get a more accurate image of the boundary. The detailed information of the combining impedance data is shown in Figure 3.7.

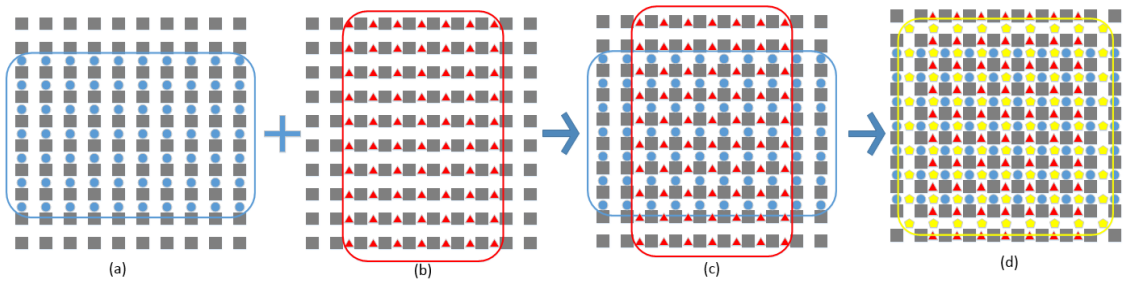

Figure 3.7: Graphical interpretation of the method of combining impedance data for horizontal and vertical scan

Circles and triangles in Figure 3.7 (a) and (b) indicate the possible impedance data point of the tetrapolar measurement method. As shown in Figure 3.7, each direction has some area where impedance data is not taken at the edge of the electrode array. Image (c) shows the graphical interpretation of combining two Z-matrices. By combining (a) and (b), the possible impedance data points can be reconstructed as in image (d). The yellow markings in image (d) were created from the average of the four surrounding measured red and blue

impedance data. Also, the missing corner data shown in image (c) was obtained from the average value data of nearby measured points. This method can compensate for the missing impedance data and it allows for a more accurate impedance mapping of the tissue boundary shape. Figure 3.8 shows the impedance mapping image of combined impedance data.

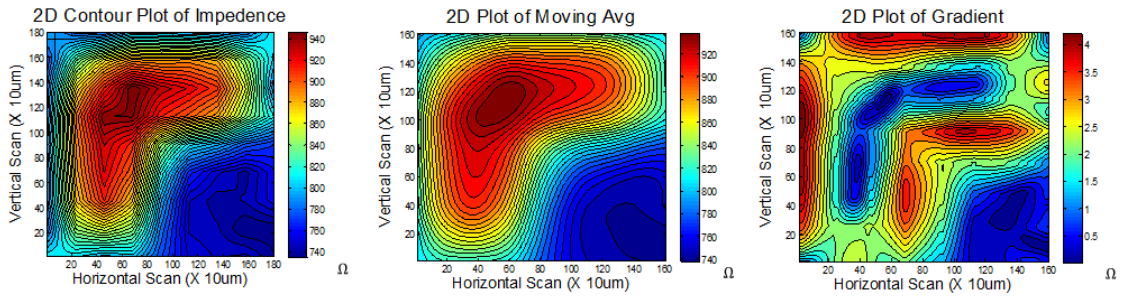

a. Image of scanned impedance change for L-shaped boundary
Distance : 100um away, Configuration : [1-4-2-3]

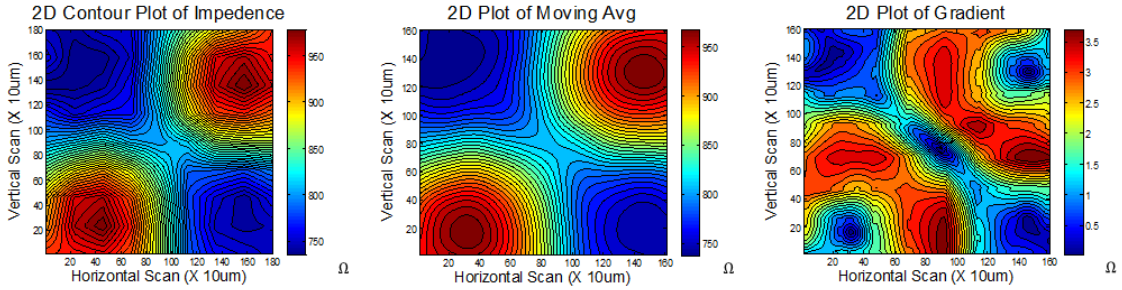

b. Image of scanned impedance change for Cylindrical-shaped boundary
Distance : 100um away, Configuration : [1-4-2-3]

Figure 3.8: The combined impedance mapping image of the different tissue boundaries detected by the electrode array

As a result of combining the horizontal and vertical scan impedance data, Figure 3.8 shows more accurate impedance mapping images compared to the spread boundary shape shown in Figure 3.6. The first image is the reconstructed impedance data (raw data) plot from the original Z-parameter matrix. The second image is a moving averaged image. In order to reduce the possible noise of raw data, the moving average data analysis has been applied. The method simply generates the averaged data subsets from the full data. In this

impedance analysis, some portion of interpolated Z-matrix was chosen and from it, the average was calculated. The second image shows the smoother image compared to the raw data image.

The third image represents the gradient image. The gradient calculation is a method to detect an abrupt change of impedance data. Performing gradient calculation allows delineating the rough edges of the tissue boundary. The row and column of the Z-matrix geometrically corresponds with the x and y axis. Then, the partial derivative of the absolute value of the impedance is taken with respect to the x and y directions. The below equation describe this relationship.

$$\nabla|\mathrm{Z(x,y)}| = \sqrt{\frac{\partial|Z(x,y)|^2}{\partial x} + \frac{\partial|Z(x,y)|^2}{\partial y}} \tag{3.1}$$

This simple computation detects any abrupt impedance change, and is able to plot the edge of the boundary shape as shown in Figure 3.8. The distance between the boundary and the electrode array model in the images shown was 100um.

As shown in Figure 3.8, it is clearly verified that the impedance sensing electrode array can detect the tumor boundary. As the first image shows, a high impedance value forms an integrated area where it matches the cross-sectional boundary shape. The moving average plot shows a smoother image than the raw image. Based on the impedance mapping image, 100um is close enough to clearly detect the boundary of the tissues with a basic 1-4-2-3 configuration. The distance then increased by 100um continuously and the data analysis has been performed with large separated electrode configurations as discussed previously. The simulation performed up to 400um which is the threshold

distance where the electrode array cannot detect the boundary. The impedance mapping images of 200um, 300um and 400um distances are shown in Figure 3.9-3.14

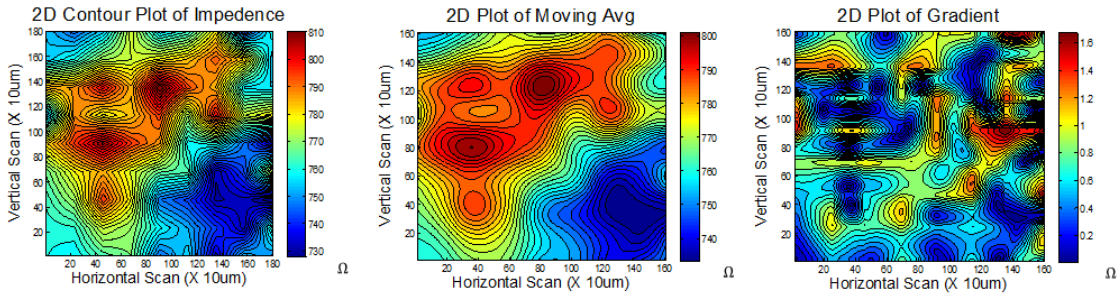

a. Image of scanned impedance change for L-shaped boundary
Distance : 200um away, Configuration : [1-4-2-3]

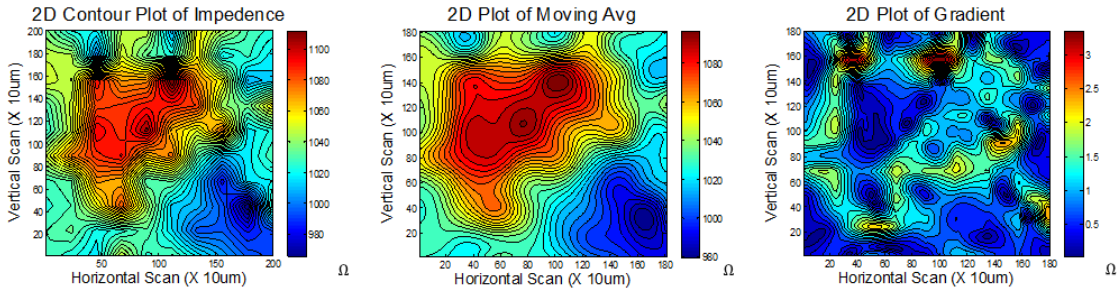

b. Image of scanned impedance change for L-shaped boundary
Distance : 200um away, Configuration : [1-5-2-4]

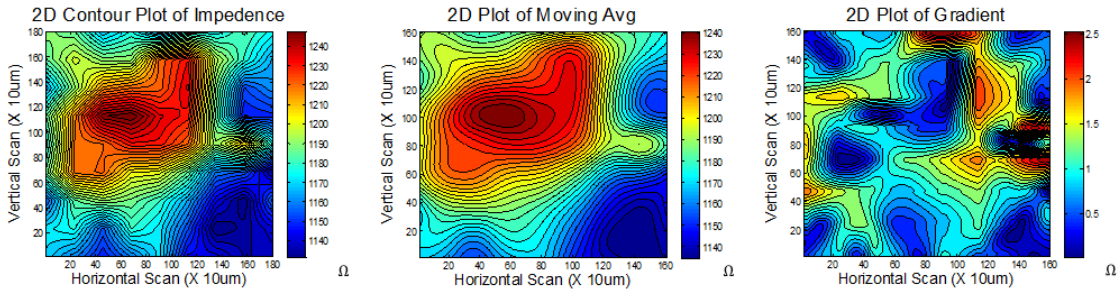

c. Image of scanned impedance change for L-shaped boundary
Distance : 200um away, Configuration : [1-6-2-5]

Figure 3.9: Impedance mapping image of L-shaped boundary measured from 200um distance

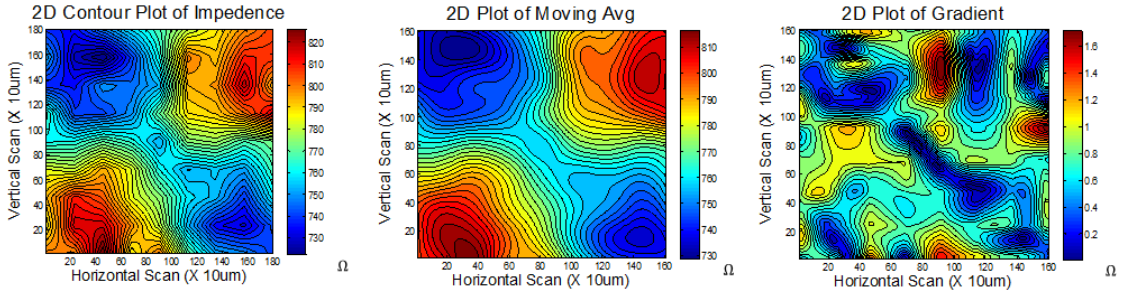

a. Image of scanned impedance change for Cylindrical-shaped boundary
Distance : 200um away, Configuration : [1-4-2-3]

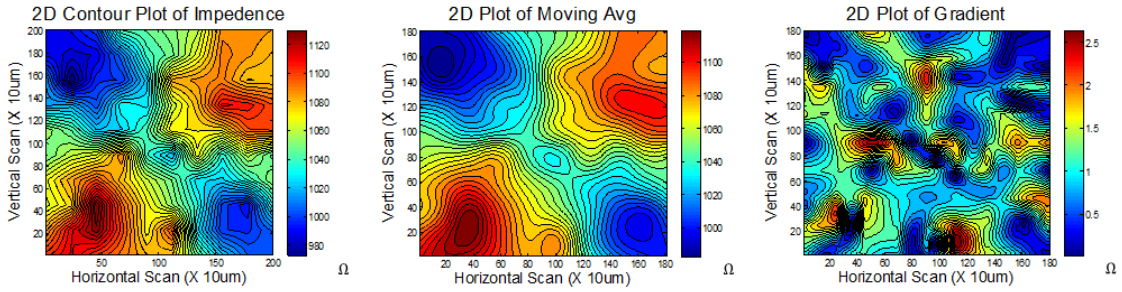

b. Image of scanned impedance change for Cylindrical-shaped boundary
Distance : 200um away, Configuration : [1-5-2-4]

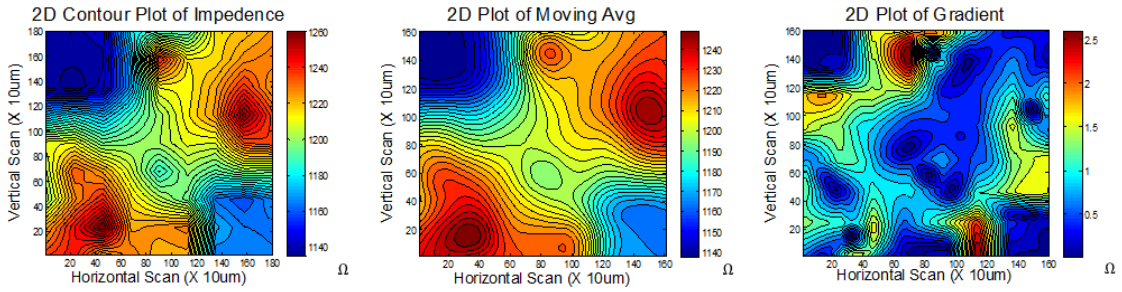

c. Image of scanned impedance change for Cylindrical-shaped boundary
Distance : 200um away, Configuration : [1-6-2-4]

Figure 3.10: Impedance mapping image of Cylindrical-shaped boundary measured from 200um distance

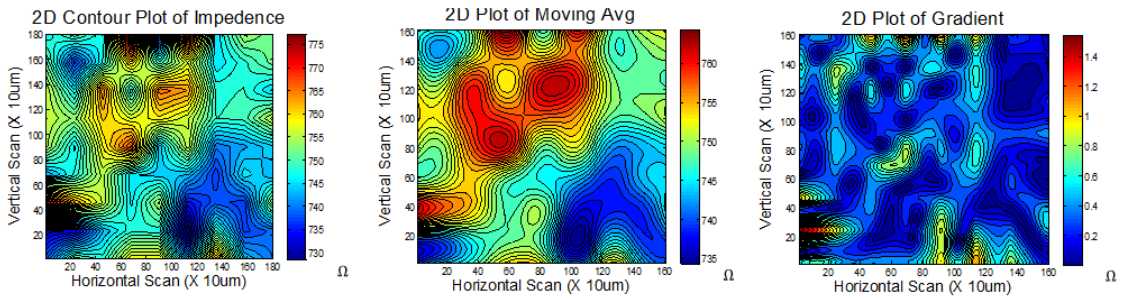

a. Image of scanned impedance change for L-shaped boundary
Distance : 300um away, Configuration : [1-4-2-3]

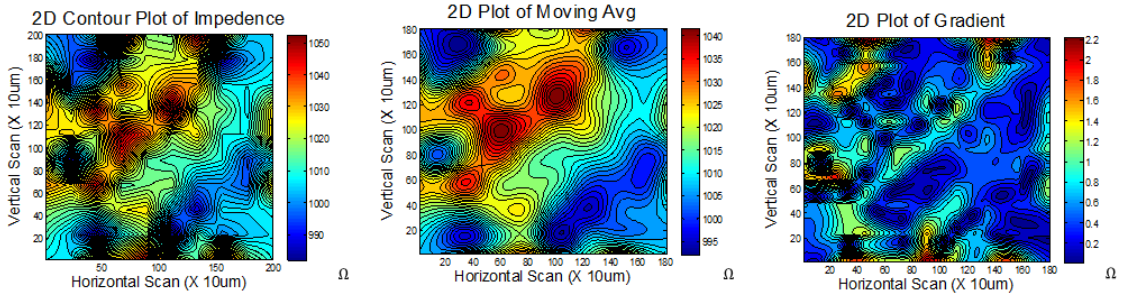

b. Image of scanned impedance change for L-shaped boundary
Distance : 300um away, Configuration : [1-5-2-4]

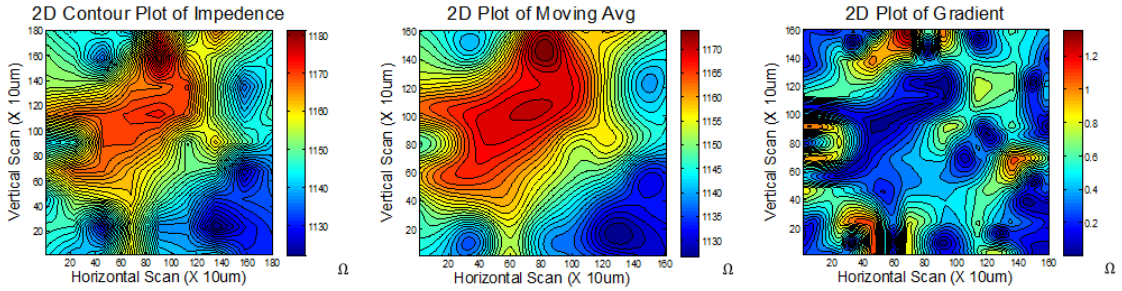

c. Image of scanned impedance change for L-shaped boundary
Distance : 300um away, Configuration : [1-6-2-5]

Figure 3.11: Impedance mapping image of L-shaped boundary from 300um distance

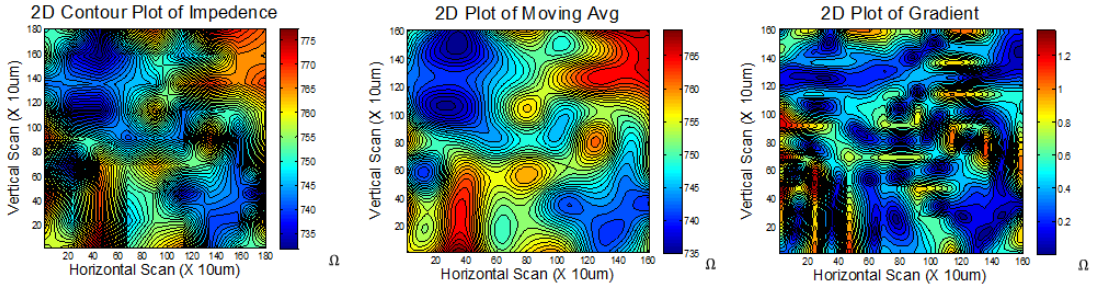

a. Image of scanned impedance change for Cylindrical-shaped boundary
Distance : 300um away, Configuration : [1-4-2-3]

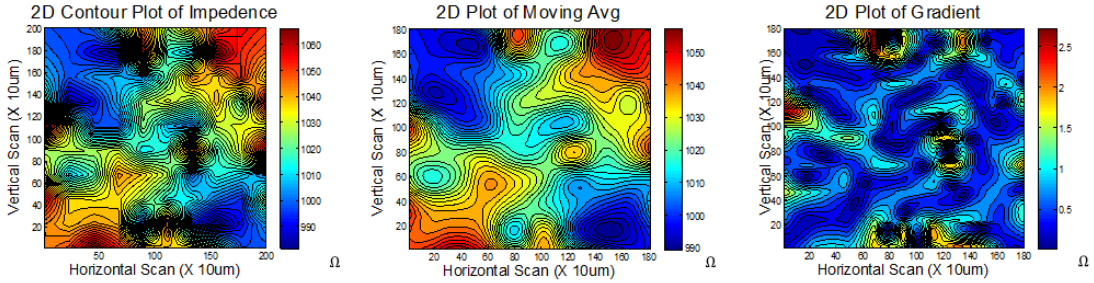

b. Image of scanned impedance change for Cylindrical-shaped boundary
Distance : 300um away, Configuration : [1-5-2-4]

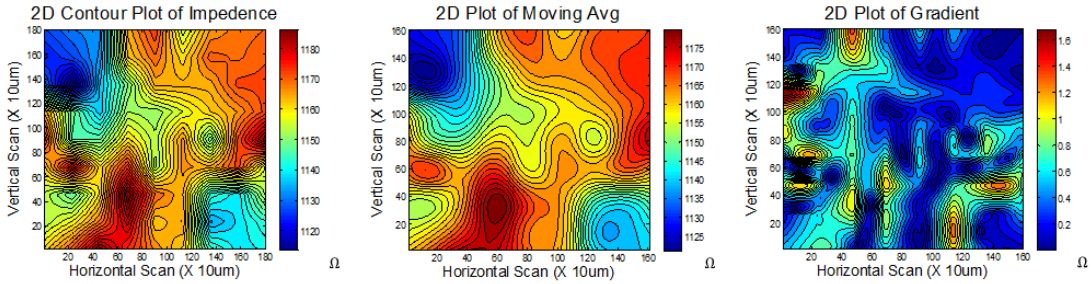

c. Image of scanned impedance change for Cylindrical-shaped boundary
Distance : 300um away, Configuration : [1-6-2-5]

Figure 3.12: Impedance mapping image of Cylindrical-shaped boundary measured from 300um distance

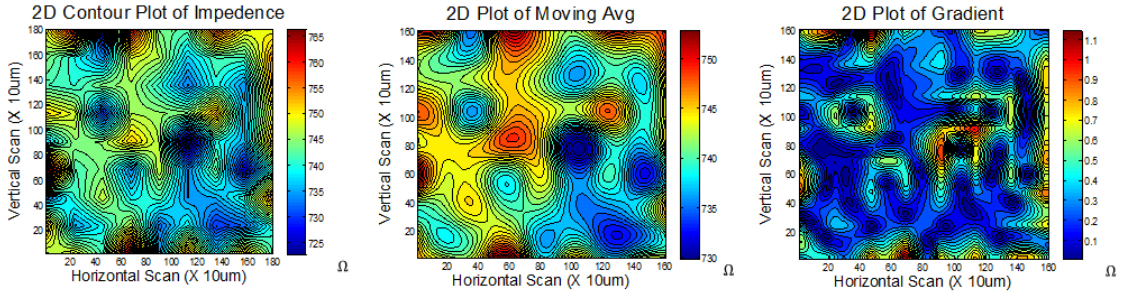

a. Image of scanned impedance change for L-shaped boundary
Distance : 400um away, Configuration : [1-4-2-3]

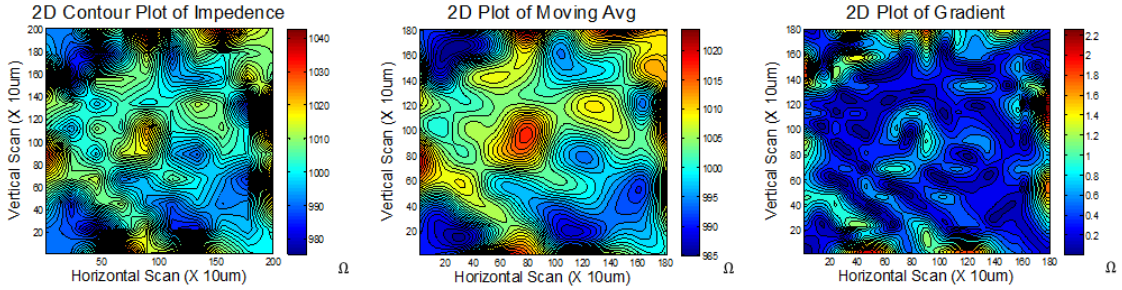

b. Image of scanned impedance change for L-shaped boundary
Distance : 400um away, Configuration : [1-5-2-4]

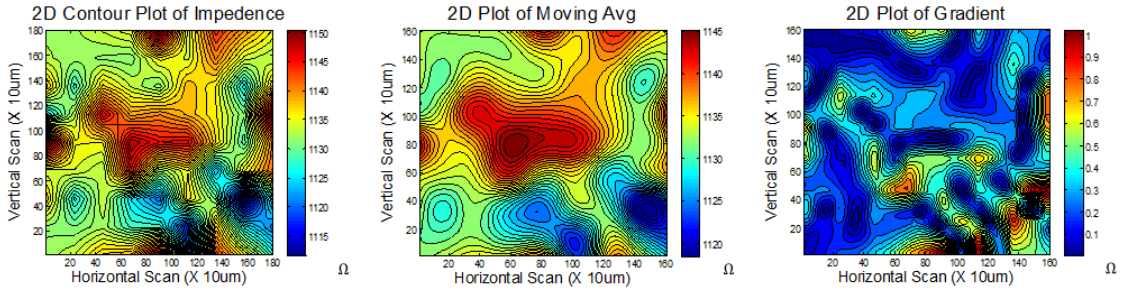

c. Image of scanned impedance change for L-shaped boundary
Distance : 400um away, Configuration : [1-6-2-5]

Figure 3.13: Impedance mapping image of L-shaped boundary measured from 400um distance

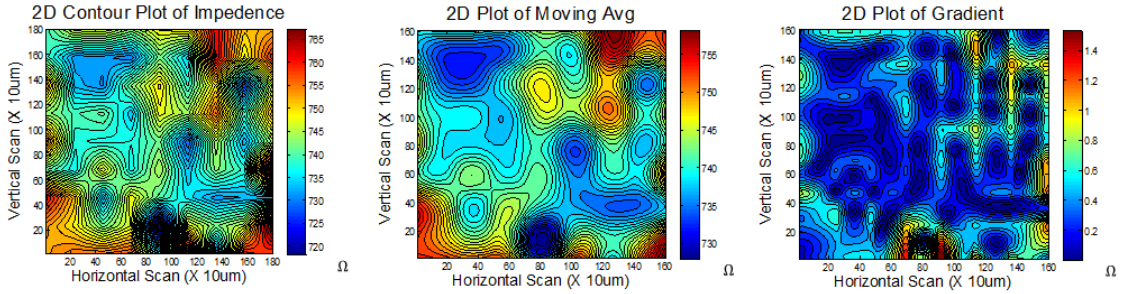

a. Image of scanned impedance change for Cylindrical-shaped boundary
Distance : 400um away, Configuration : [1-4-2-3]

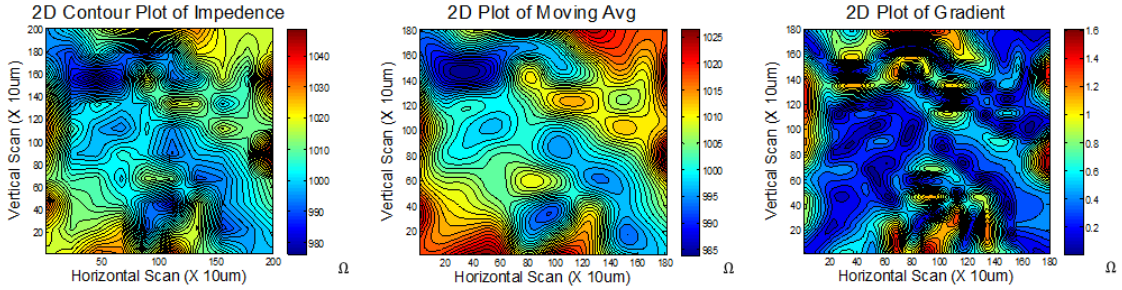

b. Image of scanned impedance change for Cylindrical-shaped boundary
Distance : 400um away, Configuration : [1-5-2-4]

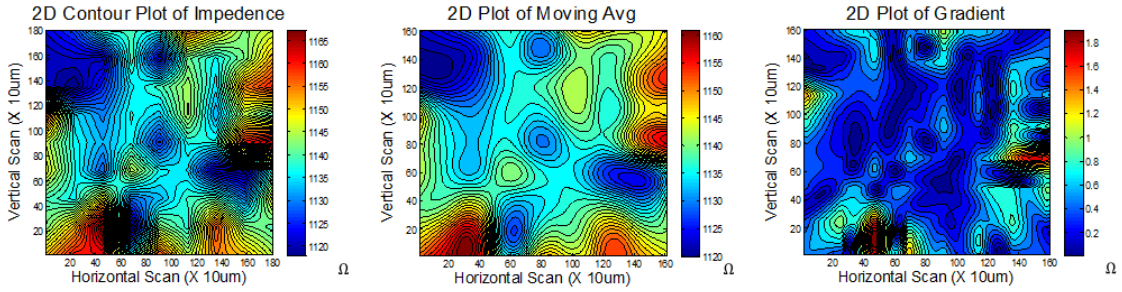

c. Image of scanned impedance change for Cylindrical-shaped boundary
Distance : 400um away, Configuration : [1-6-2-5]

Figure 3.14: The impedance mapping image of Cylindrical-shaped boundary measured from 400um

Figures 3.9-3.14 demonstrate the impedance mapping image generated from different distances with different configurations. The same cylindrical and L shaped boundaries are plotted sequentially and the 1-4-2-3, 1-5-2-4 and 1-6-2-5 electrode configuration scanning has been plotted together for each distance.

At 200um, the system can still roughly map out the tumor boundaries for all configurations. Although the exact cylindrical and L shaped images cannot be clearly distinguished as in the 100um distance case, the image was clear enough for a rough estimation of the boundary shape. However, the gradient plots do not exactly match with the edge of the boundary. Since the gradient plot detects the abrupt changes of the impedance, it is only useful when the clear boundary image can be detected as in the 100um case.

For the 300um case, the 1-4-2-3 configuration barely detects the tissue boundary but as the configuration changes (1-5-2-4 and 1-6-2-5), a more clear high impedance region is detected although the exact shape is unclear. At this point, it is hard to distinguish the shape of the boundary, but the clear impedance variation allows the estimation of the possible distance to the boundary edges from the electrode array.

At the 400um distance, all the configurations start to show an ambiguous image of the boundary. Although a large electrode selection image shows a high impedance area, it is impossible to define the shape of the boundary. However, as the 300um results show, the large electrode selection can roughly estimate the distance from the tissue boundary to the electrode array.

As the configuration changes, the resolution of the boundary detection is significantly reduced and there is missing impedance data at the corner as described in Figure 3.7.

In addition to a reduction in resolution, the large current conduction area causes inaccurate impedance measurements of the two different tissues. The estimating distance from the boundary to the electrode can be estimated with large electrode separation but the boundary shape detection is difficult. The large number of electrode array would give better resolution and result in more precise boundary detection.

3.3 Demonstration based on 3-D MRI Derived Brain Model

For a more realistic approach, an MRI derived 3D finite element brain model was generated. The 3D brain model was generated from high resolution MRI scanned images by SIMPLEWARE(LTD., UK). Figure 3.15 shows the procedure to create a 3D brain model. A total of 186 image slices of DICOM format 1mm thick MRI images of the human head were provided from the University of Kentucky. The volumetric brain model was generated through segmenting each slice and the irregular tumor model was also segmented. The dimensions of the brain are 120 mm × 170 mm × 90 mm (width × length × height) and the dimensions of the tumor are 25mm × 30mm × 18mm. The detailed parts of the human brain such as the skull, the cerebellum, the spinal cord, or the brain stem were not fully extracted for simplicity.

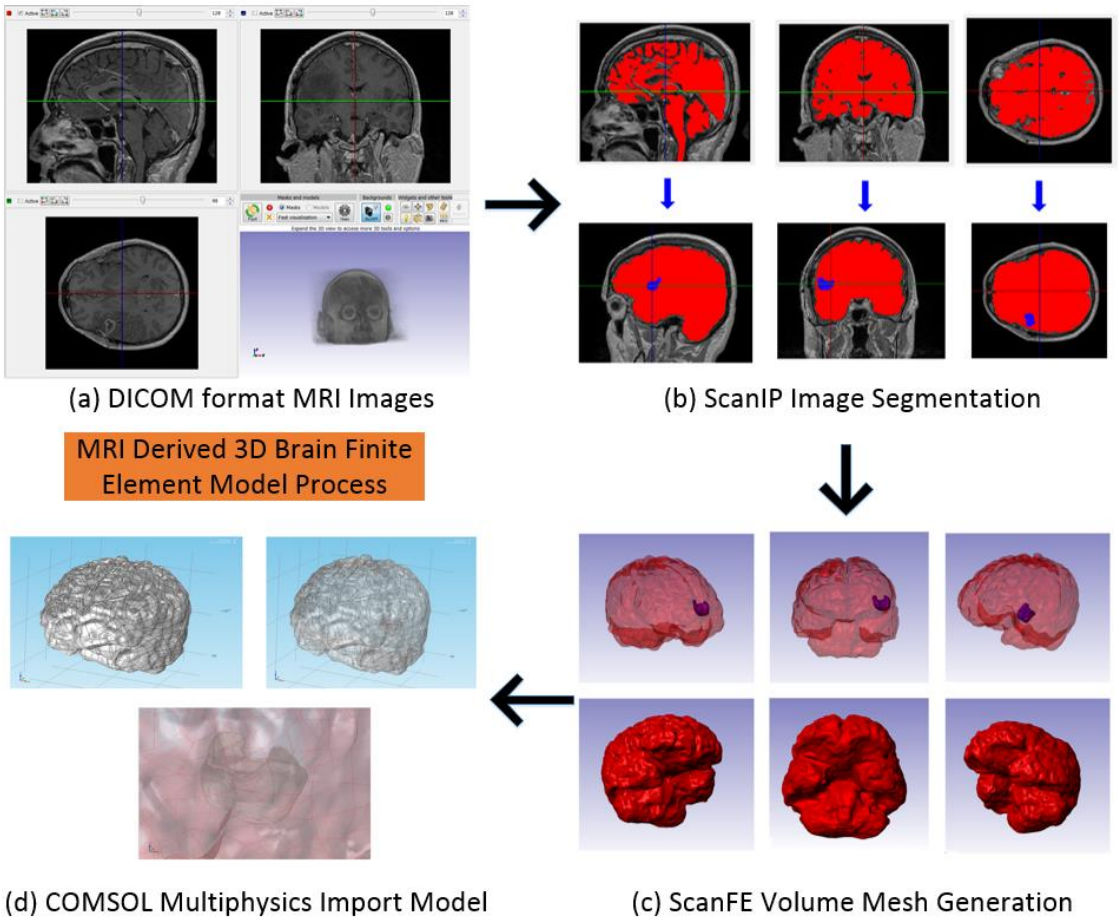

Figure 3.15: The sequence of the finite element model image process by SIMPLEWARE (LTD,, UK)

The detailed surface of the brain was filtered and smoothed because the complex geometry could not be meshed in COMSOL Multiphysics® causing an error when it was simulated. As shown in Figure 3.15, the brain and the tumor (blue part) were segmented by the ScanIP image processing and transformed into a 3D volumetric geometry through the ScanFE module. Afterwards, the geometry is finally imported into COMSOL Multiphysics®. The final geometry meshed in COMSOL Multiphysics ® consists of 1,209,881 domain elements, 147,980 boundary elements and 23,022 edge elements. The material setup was the same as in the previous simple model. The same healthy and tumor material were

assigned to the new brain and tumor model, respectively. Once the brain model is imported into COMSOL Multiphysics®, the electrode array model was placed inside the tumor as shown in Figure 3.15 (d). The detailed picture is shown below in Figure 3.14

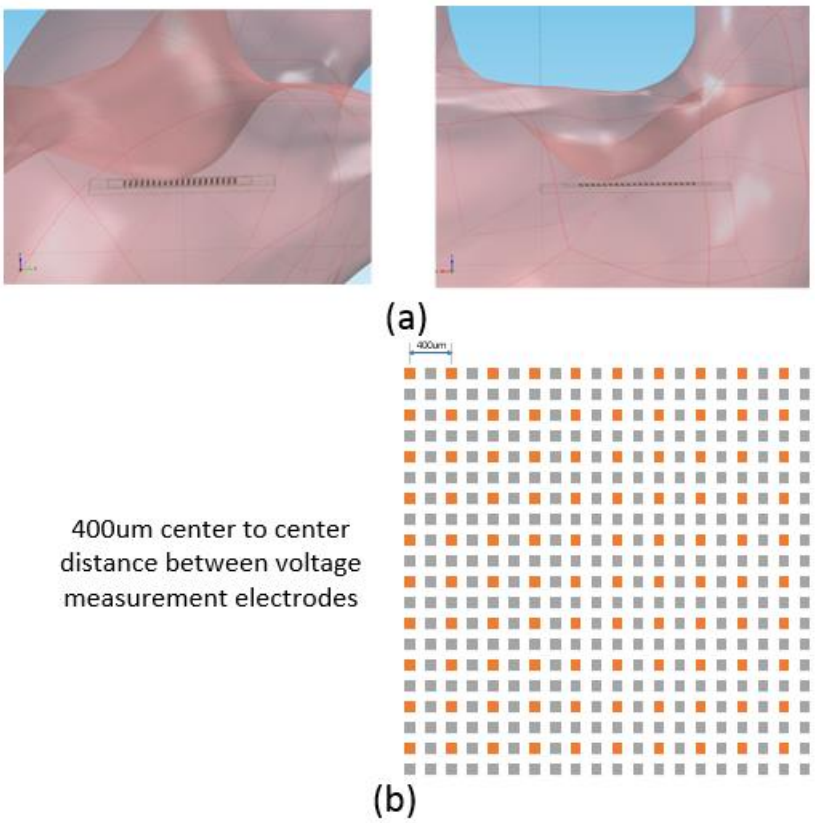

Figure 3.16: (a) simulation setup of tumor and the electrode array at the boundary. (b) 20×20 Electrode array with 100 terminals sparsely selected

As shown in Figure 3.16 (a), the electrode array is placed near the boundary of the tumor. The bumpy area of the tumor boundary is located at the lower left side of the electrode array. The simulation results are shown in Figures 3.17-3.18. Because of the small area covered by the 10×10 electrode array, the array was increased to 20×20. However, because of the limited computer resources, only 100 terminals out of 400 electrodes were alternatively set as shown in Figure 3.16 (b).

The brain model simulation results are shown in Figures 3.17-3.18. As the previous simple verification shows, the tissue boundary is mapped with the impedance difference between two regions detected by the lower left side of the electrode array. The shape and the location are perfectly matched with the simulation model. Since the electrodes are sparsely selected, the model was the same as with the largely separated electrode configurations. Thus, the model should be able to detect the boundary from a further distance than the previous model. In case of the previous cylindrical and L shaped boundary simulation, the clear mapping image is shown only from 100um distance and the boundary is no longer detected beyond 400um. However, the brain simulation electrode array model shows a clear boundary shape even for the 300um and 400um distances. Figures 3.17-3.18 include the 1-5-2-4 configuration, but the 1-4-2-3 configuration is enough to detect the boundary at all distances. The 1-5-2-4 configuration shows a more distorted image than the 1-4-2-3 configuration. This indicates that there is an optimum configuration for each distance that enables the best impedance mapping of the tissue boundary.

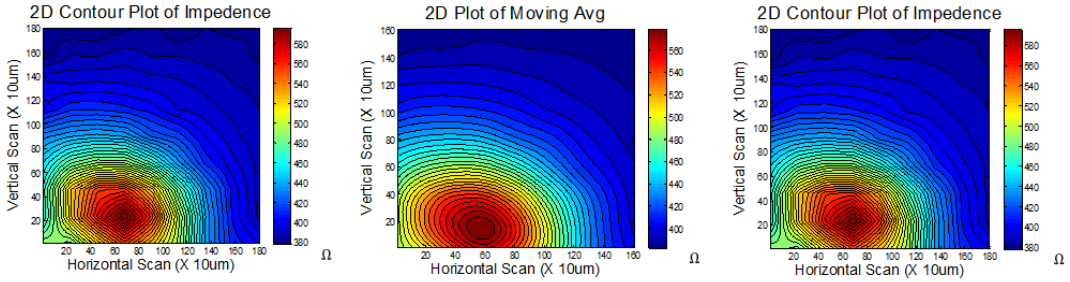

Figure a. Image of scanned impedance change for MRI derived brain model
Distance : 100um away, Configuration : [1-4-2-3]

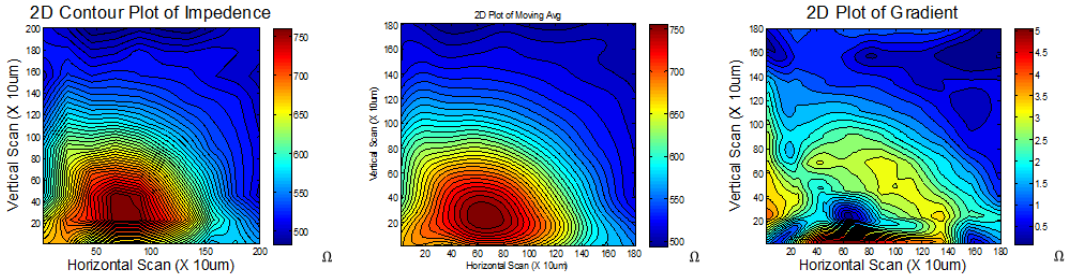

Figure b. Image of scanned impedance change for MRI derived brain model
Distance : 100um away, Configuration : [1-5-2-4]

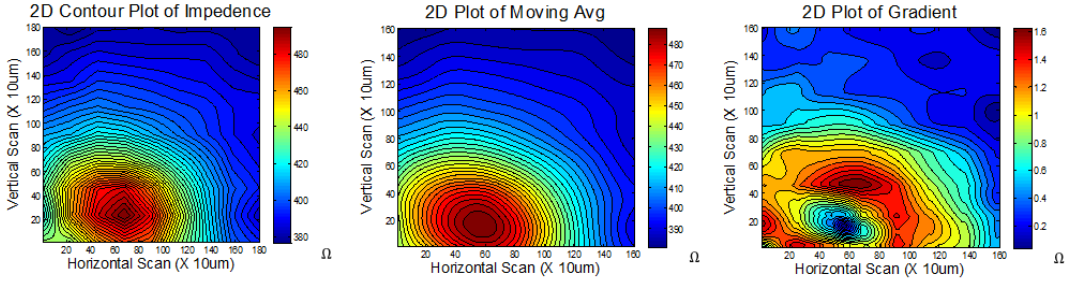

Figure a. Image of scanned impedance change for MRI derived brain model
Distance : 200um away, Configuration : [1-4-2-3]

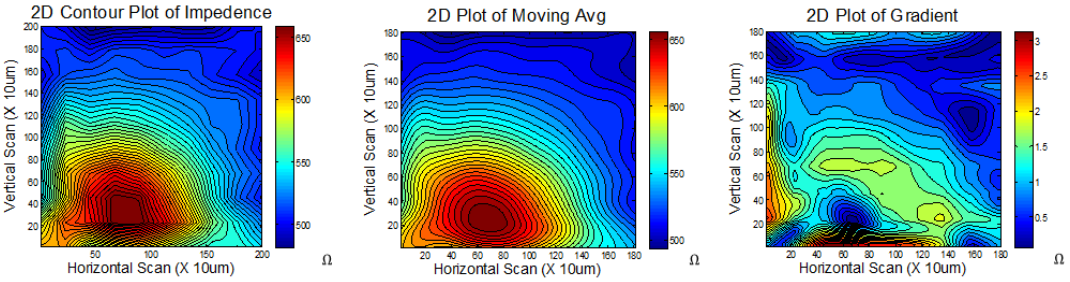

Figure b. Image of scanned impedance change for MRI derived brain model
Distance : 200um away, Configuration : [1-5-2-4]

Figure 3.17: Impedance mapping image of MRI derived brain model measured from 100um and 200um distance

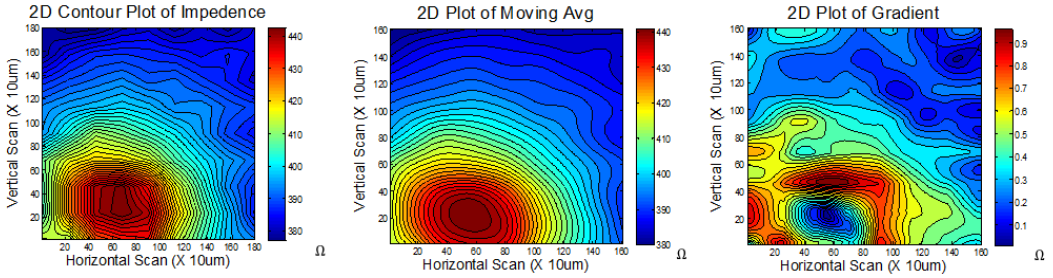

Figure a. Image of scanned impedance change for MRI derived brain model
Distance : 300um away, Configuration : [1-4-2-3]

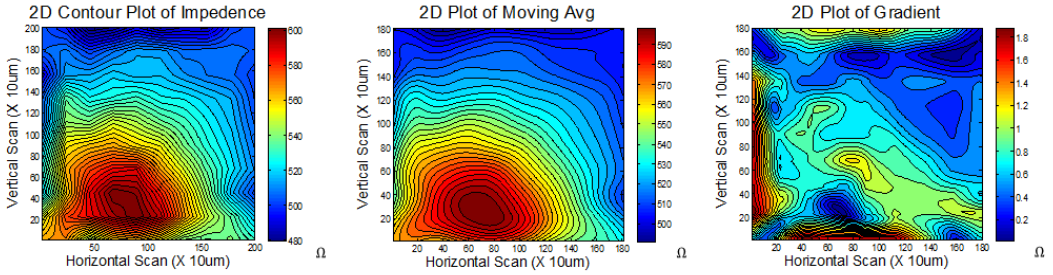

Figure b. Image of scanned impedance change for MRI derived brain model
Distance : 300um away, Configuration : [1-5-2-4]

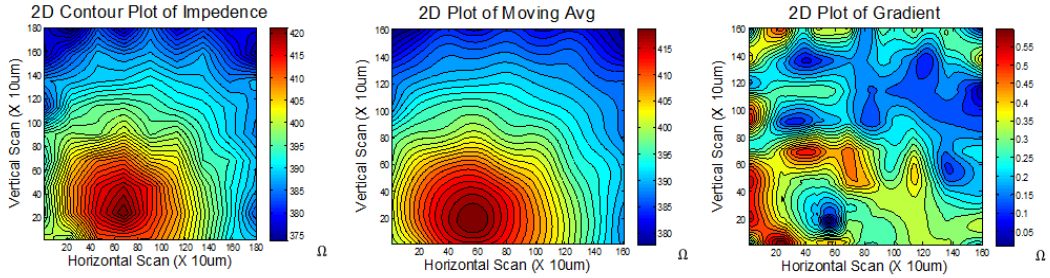

Figure a. Image of scanned impedance change for MRI derived brain model
Distance : 400um away, Configuration : [1-4-2-3]

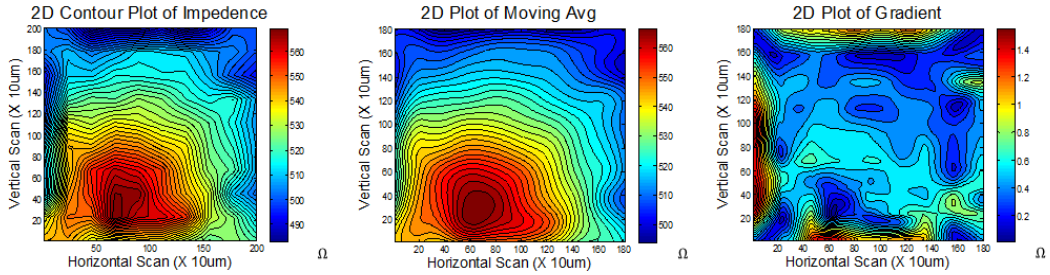

Figure b. Image of scanned impedance change for MRI derived brain model
Distance : 400um away, Configuration : [1-5-2-4]

Figure 3.18: Impedance mapping image of MRI derived brain model measured from 300um and 400um distance

CHAPTER 4

PCB IMPEMENTATION OF AN ELECTRICAL IMPEDANCE SENSOR

4.1 Impedance Sensor Array Circuit

The proposed impedance mapping sensor array has been verified by the previous simulation. As the next step, the system level design was performed with a PCB-level implementation. The PCB level system implementation is a proof-of-concept design.

4.1.1 System Level Overview

As previously discussed, the electrode array improves the sensing mechanism from a single data point to impedance mapping image of tissues boundary. The proposed concept is verified by simulation and the real impedance mapping system has been built at a PCB level. The overall system is shown in Figure 4.1.

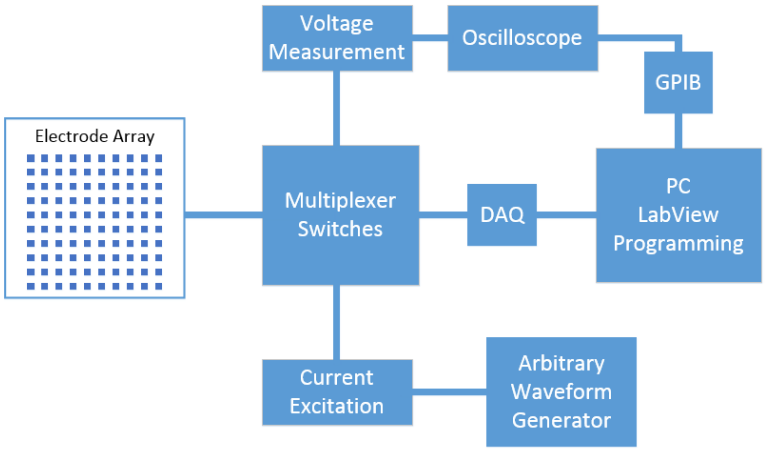

Figure 4.1: Automated electrode array impedance measurement system

To get the detailed information of the boundary, measurements have to be taken in various configurations, and the correct impedance data analysis is important. A current source and a voltage measurement circuit have to have access to any electrode. Multiplexers are used as switches to direct the electrode configuration to the circuits. The multiplexer switching is controlled by binary bits produced from a USB-Digital I/O device (DAQ). NI LabView is used to produce the binary address for the multiplexer and programmed to enable automatic measurement system. A modified Howland current circuit is used as the current source and the voltage input is taken from an Arbitrary Waveform Generator. For the voltage measurement, an instrumentation amplifier was designed, and the output single-ended output voltage is measured by the oscilloscope.

4.1.2 Current Sourcing Circuit

For the tetrapolar impedance measurement method, a constant current generation is an essential factor because the impedance is directly related to the ratio of the known current and the voltage measured. Therefore, the current sourcing circuit has to produce a constant current which would not be affected by load variations over a wide range of frequencies. A Voltage-Controlled-Current-Source (VCCS) is normally used for impedance measurement. It takes a sinusoidal voltage input and produces an alternating constant current output. A simple current source analysis is shown in Figure 4.2.

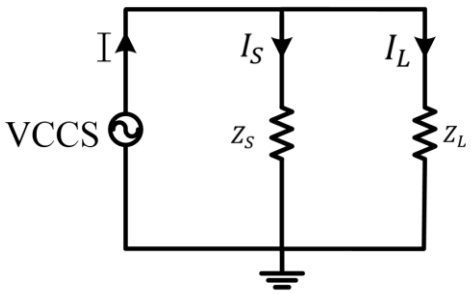

Figure 4.2: A simple current source model with load Z_L and the output impedance Z_s presented. Ideal current source has infinite Z_s, so that the load current I_L is the same as total current I

The total current is I and Z_s is the internal output resistance of the current source. The circuit can be simply analyzed in that if Z_S goes infinitely high, the current $I_L = I$. The output impedance of the current circuit is the most important factor to produce the constant current. There are many types of VCCS circuit designs proposed from previous research, but there are two major VCCS designs for bioelectrical impedance measurements. Those include a modified Howland circuit (Texas Instruments 2008 and Bertemes-Filho 2002) and current mirror architecture (Casas et al., 1996 and Wilson, 1981). The modified Howland circuit has been chosen for this project since it is relatively simple to design and the performance is not much different from the current mirror architecture. Bertemes-Filho (2002) used the modified Howland circuit to design the impedance mapping system and compared its performance with that of the current mirror architecture. The modified Howland Circuit schematic is shown in Figure 4.3.

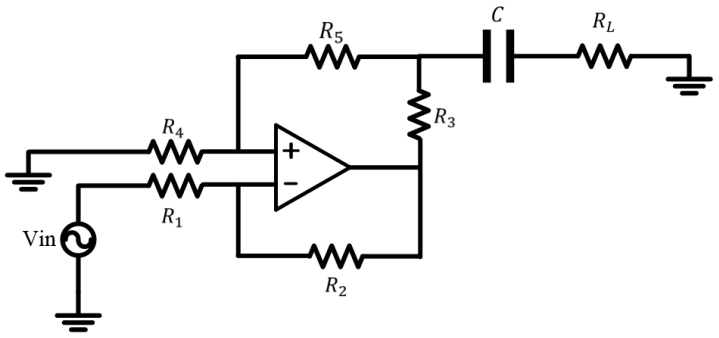

Figure 4.3: Schematic of a modified Howland current sourcing circuit using both positive and negative feedback

The circuit takes the voltage input and produces the current output. The transfer function of the circuit can be determined as

$$I_L = \frac{R_4R_2 - R_1 \times (R_3 + R_5)}{R_1R_3 \times (R_4 + R_5)} \times V_L - \frac{R_2}{R_1R_3} \times V_{in} \tag{4.1}$$

To generate the constant current I_L, the V_L term has to be removed in the equation. If the first term of the equation is removed, the output current flow into the load only depends on the second term of the Equation 4.1. To remove the V_L term, the numerator of the first term should become zero, which means $R_4R_2 = R_1 \times (R_3 + R_5)$. This can be interpreted as

$$\frac{R_1}{R_2} = \frac{R_4}{(R_3 + R_5)} \tag{4.2}$$

If $R_1 = R_2$, then $R_4 = R_3 + R_5$. If this condition is satisfied, the output current is

$$I_L = -\frac{1}{R_3} \times V_{in} \tag{4.3}$$

The performance of the current source circuit mostly depends on the high output impedance of the circuit as mentioned before. The transfer function of the output impedance of the modified Howland circuit is shown below.

$$R_{out} = \frac{R_1 R_3 (R_4 + R_5)}{R_1 R_4 - R_2 R_4} \tag{4.4}$$

The output impedance of the circuit was found by circuit analysis with the input shorted and a test voltage placed at the output. As shown in Equation 4.4, as long as the condition is satisfied, the output impedance is infinite. However, the resistance cannot be perfectly matched in a real implementation. The mismatched resistor would significantly affect the output impedance of the current circuit as mentioned by the TI application note (2008); if the resistors are 10kΩ with the 1% tolerance, it would cause an output impedance variation of ±250kΩ in the worst-case.

In addition to the resistor matching, Bertemes-Filho (2012) discovered that the output impedance of the modified Howland current circuit is highly affected by the open-loop gain of the operational amplifier. Also, Bertemes-Filho (1999) performed an experiment to measure the output impedance of the modified Howland circuit, and he came to the conclusion that it is difficult to design a high output impedance (>100 kΩ) of the current sourcing circuit at high frequencies (up to 1 MHz) because of possible stray capacitance and parallel resistance connected to the output of the circuit.

The tetrapolar impedance measurement method uses a differential current source to produce positive and negative current excitations. The negative current can be generated by taking a 180 degree phase-shifted negative voltage input by another modified Howland

circuit. Figure 4.4 shows a simple circuit that takes the single ended input and produces a differential output signal. The differential signal generator circuit is shown in Figure 4.4.

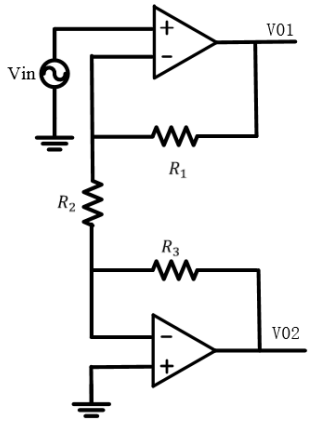

Figure 4.4: Schematic of single ended input to differential output generator circuit

The circuit can be simply analyzed by the following equations.

$$V_{01} = V_{in}\left(1 + \frac{R_1}{R_2}\right) \tag{4.5}$$

$$V_{01} = -V_{in}\left(\frac{R_3}{R_2}\right) \tag{4.6}$$

$$If\ 1 + \frac{R_1}{R_2} = \frac{R_3}{R_2}\ and\ R_2 + R_1 = R_3 \tag{4.7}$$

$$V_{01} = V_{in}\left(\frac{R_3}{R_2}\right)\ and\ V_{02} = -V_{in}\left(\frac{R_3}{R_2}\right) \tag{4.8}$$

As long as the Equation 4.7 is satisfied, the circuit produces a differential voltage signal at its output. The differential output of the circuit then was connected to two modified

Howland circuits. The final differential modified Howland circuit schematic is shown in Figure 4.5.

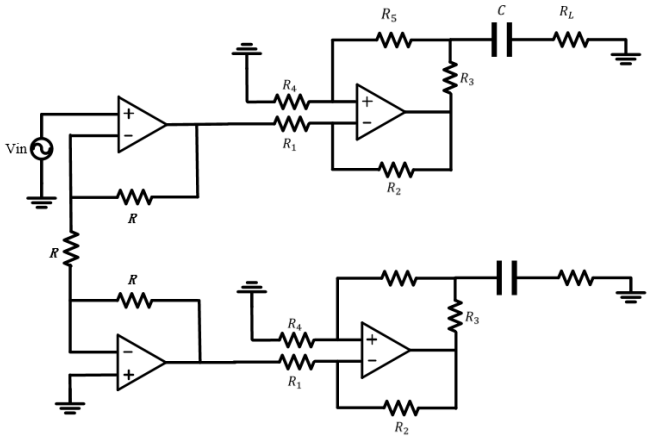

Figure 4.5: The full schematic of the differential modified Howland circuit

The performance of the modified Howland circuit was simulated by OrCAD Capture from Cadence. The PSPICE simulation model was downloaded from the Texas Instruments website and the model was imported into the OrCAD library. Figure 4.6 shows the OrCAD schematic of the differential modified Howland circuit.

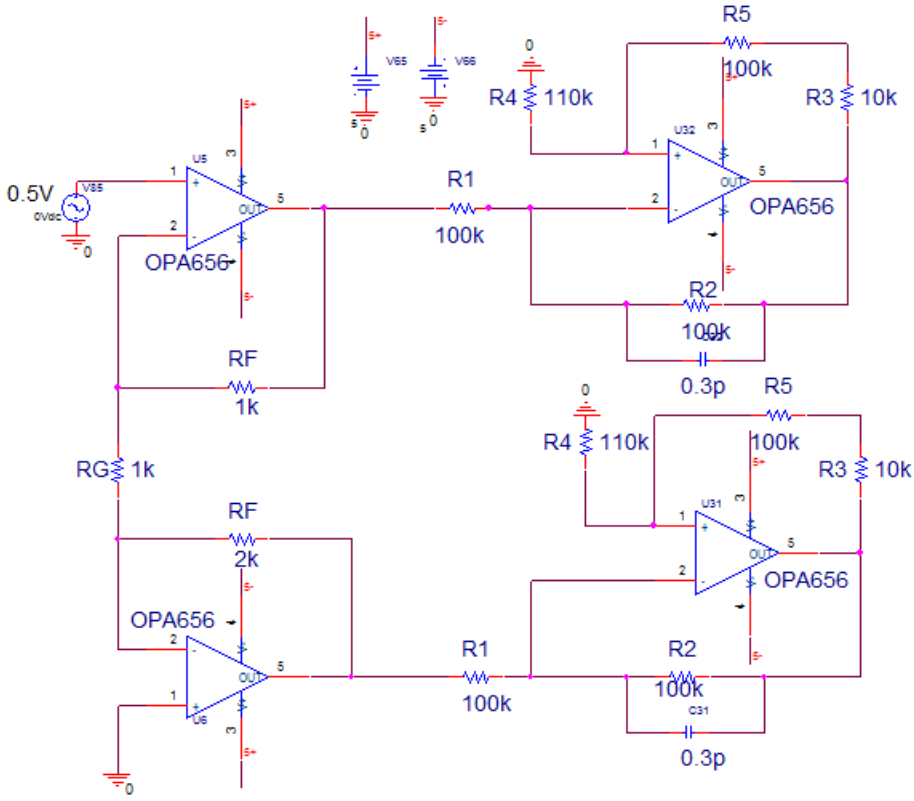

Figure 4.6: OrCAD Capture simulation schematic of the differential modified Howland Circuit

As discussed in Equation 4.3, the amount of current generation depends on the input signal and resistor R_3. To generate a 100uA output current, amplitude of 1V input signal was supplied to the input of the modified Howland circuit and R_3 was set to be 10kΩ. Other resistor and capacitor values are shown in Figure 4.6 schematic. The AC and transient simulation were performed and the resulting images are shown in Figure 4.7.

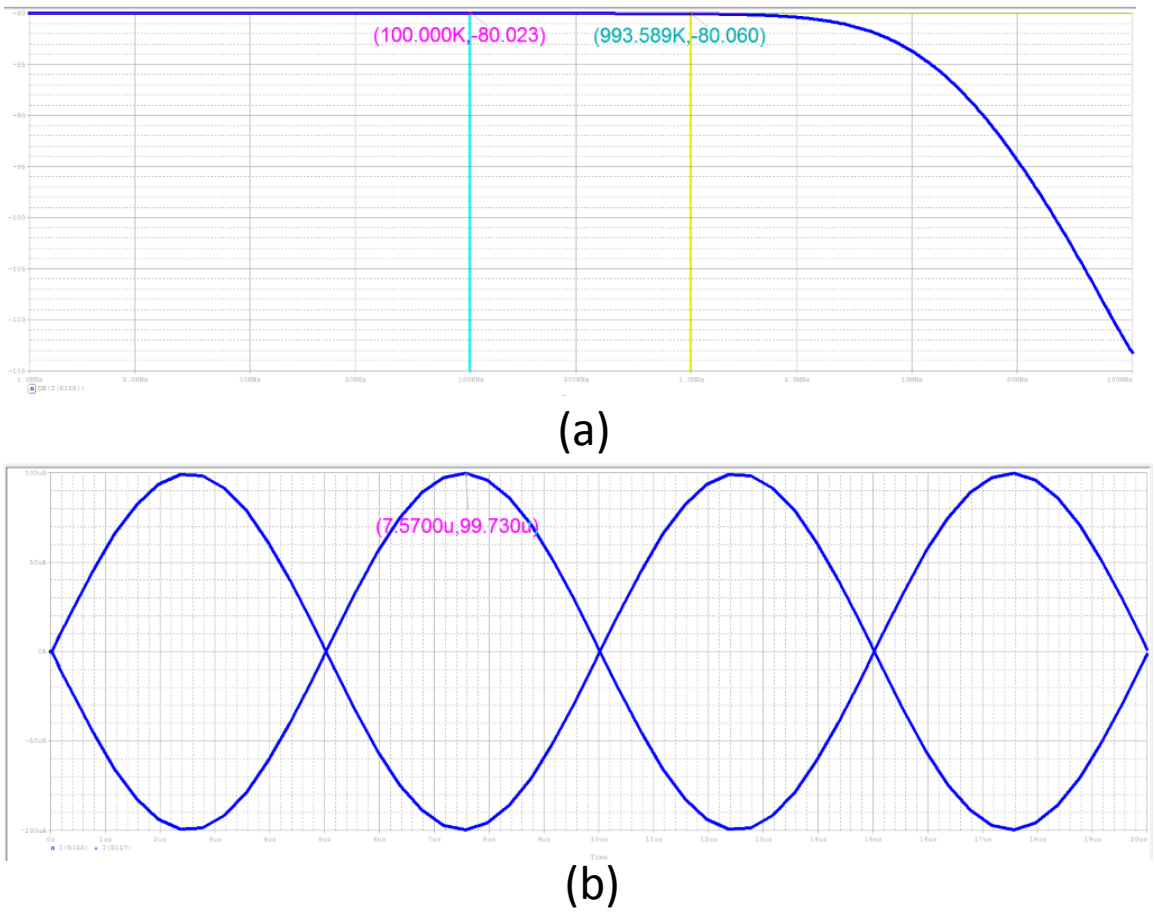

Figure 4.7: The differential modified Howland circuit simulation results. (a) AC simulation (b) Transient simulation

As shown in Figure 4.7 (a), the gain of the current source circuit is -80 dB and operates up to 1MHz. After 1 MHz, the performance of the circuit starts degrading. Graph (b) is the transient analysis measured from each output of two differential outputs of the circuit. The 180 degree phase-shifted sinusoidal signals were produced with 100uA amplitude as designed.

4.1.3 Voltage Measurement Circuit

Ideally, the AC voltage signal should be measured with minimum noise and minimum common mode signal from the tissues (Bertemes-Filho 2002). To reduce interference, an instrumentation amplifier is used to measure the potential voltage because the instrumentation amplifier has high input impedance, high Common-Mode-Rejection-Ratio (CMRR) and low noise. The typical instrumentation amplifier consists of two pre-amplifiers at the first stage and one amplifier at the second stage. The schematic of the instrumentation amplifier is shown in Figure 4.8 (Thomas 2005).

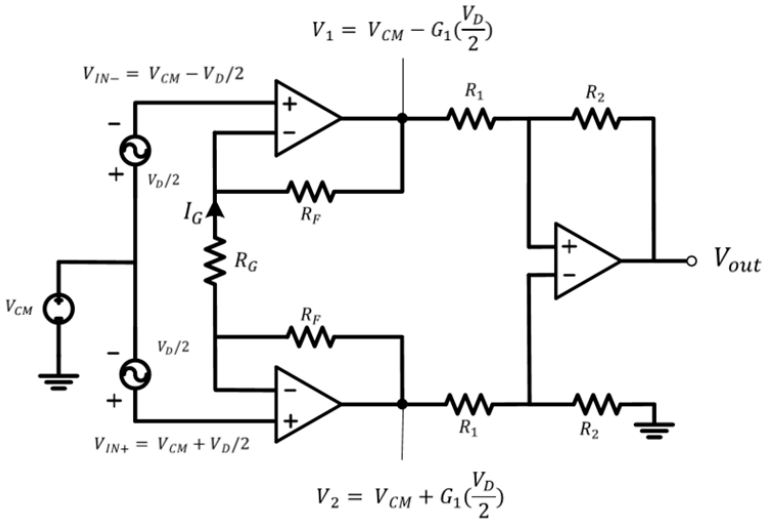

Figure 4.8: Schematic of the instrumentation amplifier

The gain of the amplifier is determined by R_G at the first stage and the second stage is just an inverting amplifier, which is the stage where the common mode signal is removed. The equation is as following,

$$R_G = \frac{V_{IN+} + V_{IN-}}{R_G} = \frac{V_D}{R_G} \tag{4.9}$$

$$V_1 = V_{CM} - \frac{V_D}{2} - I_G R_F \; and \; V_2 = V_{CM} + \frac{V_D}{2} + I_G R_F \tag{4.10}$$

$$V_1 = V_{CM} - \frac{V_D}{2}\left(1 - 2\frac{R_F}{R_G}\right) and \; V_2 = V_{CM} + \frac{V_D}{2}\left(1 + 2\frac{R_F}{R_G}\right) \tag{4.11}$$

$$V_1 = V_{CM} - \frac{V_D}{2} G_1 and \; V_2 = V_{CM} + \frac{V_D}{2} G_1 \left(where \; G_1 = 1 + 2\frac{R_F}{R_G} \right) \tag{4.12}$$

$$V_{out} = (V_2 - V_1) G_2 \left(where \; G_2 = \frac{R_2}{R_1} \right) \tag{4.13}$$

As shown in the Equation 4.12 only the differential signal is amplified by gain G_1 at the first stage. The gain of the first stage only depends on the R_F and the R_G resistors. Since the output voltage swing capability of the instrumentation amplifier is limited by the operational amplifier, the gain cannot be too high if the tissue impedance is higher than a few kΩ. Once the R_F value is set, the gain can be adjusted by changing R_G. Because the PCB design has the flexibility of adjusting resistor values, the gain was designed to be about 20 dB in the first design. The common mode signal is then removed at the second stage as shown in Equation 4.13. The performance of the instrumentation amplifier is simulated by OrCAD Capture. The circuit is implemented with an OPA657 operational amplifier by Texas Instruments. The OrCAD schematic of the instrumentation amplifier is shown in Figure 4.9.

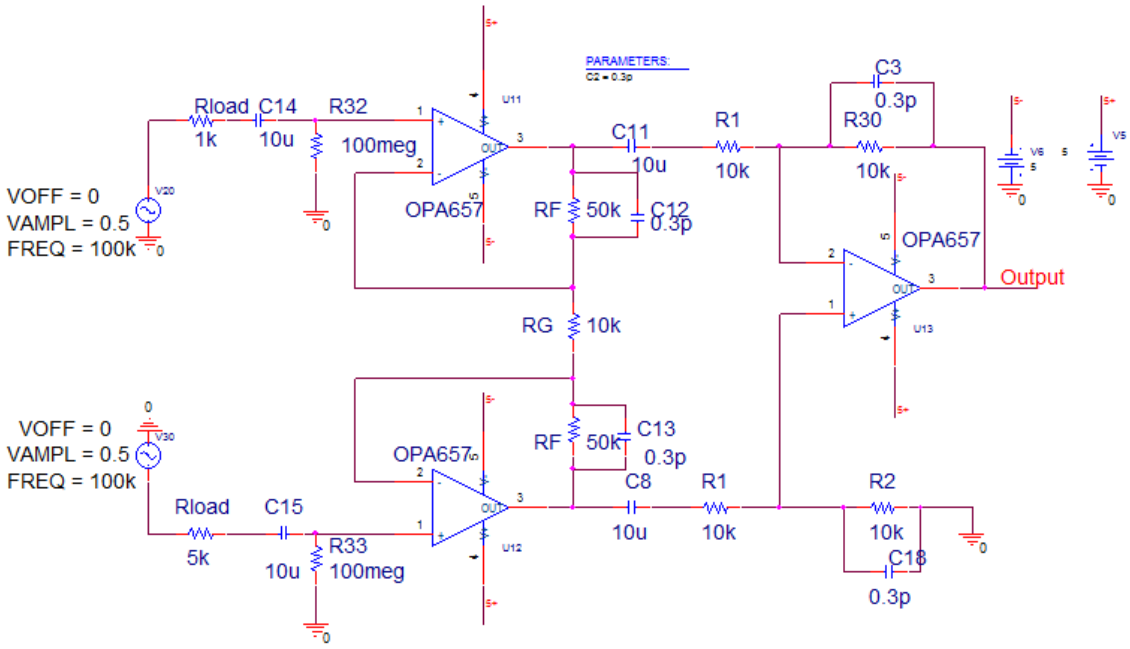

Figure 4.9: OrCAD Capture simulation schematic of the instrumentation amplifier

The resistors at the input are considered as the tissue. The DC blocking capacitors and the resistors were placed as high pass filter to block the low frequency signal at the input of the circuit. The compensation capacitors are connected in parallel to the resistor to prevent possible oscillation. The simulation results are shown in Figure 4.10

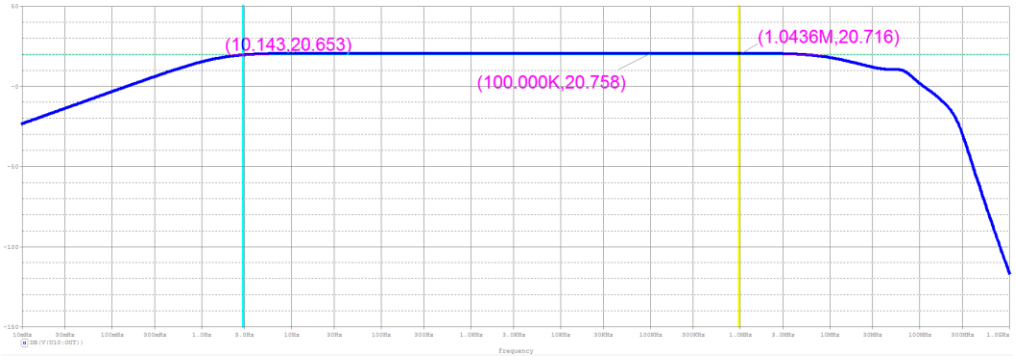

Figure 4.10: AC simulation result for the instrumentation amplifier (frequency vs dB)

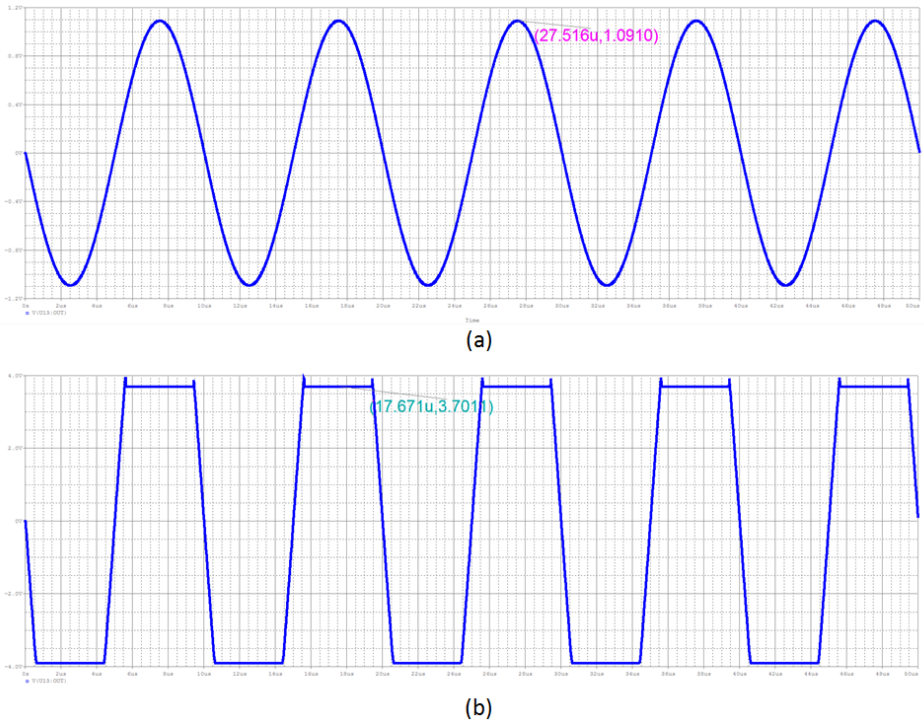

Figure 4.11: Transient simulation result of the instrumentation amplifier

The amplitude of the AC signal is 0.5 V with 100 kHz frequency. This signal was injected and the gain shows 20 dB as shown in Figure 4.8. All resistors at the second stage were chosen as 10 k**Ω**, so that the gain of the second stage is unity.

Figure 4.11 (a) shows transient analysis of the circuit. It shows the pure sinusoidal output signal at 100 kHz. The Figure 4.11 (b) graph shows the clipped sinusoidal graph. The gain was set to be 20dB, which means that the signal was amplified by 11 times the input signal 0.5V. Thus, the amplitude of the output signal exceeded the output swing capability of the op-amp, thus the signal was clipped. The input signal was then reduced to 0.05V, and the output signal showed a clear amplified sinusoidal voltage signal with a magnitude of 1.1V. The second stage is a differential inverting amplifier with unity gain whose purpose is to reject the common mode signal.

4.2 Automated Measurement Multiplexer System

The size of the electrode array implemented with the PCB was 10 × 10, which contain a total of 100 electrodes. To select all the different configurations and enable the scanning method of the electrode array, the multiplexers are used as switches to make connections between the circuits and the electrode array. ADG1406 from Analog Device has been chosen since it has enough channels (16 inputs) and 9.5Ω on-resistance. TSSOP and LFCSP pin configurations were available for the ADG1406 multiplexer. TSSOP pin configuration has been chosen to build the system. The 16 channels can be switched to one output by controlling the binary address (A0, A1, A2 and A3). Figure 4.12 shows the pin configuration of the TSSOP type and the corresponding truth table.

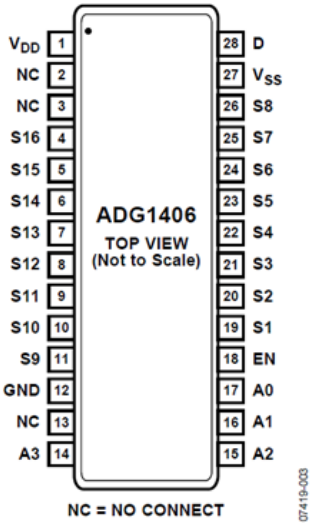

(a)

A3	A2	A1	A0	EN	On Switch
X	X	X	X	0	None
0	0	0	0	1	1
0	0	0	1	1	2
0	0	1	0	1	3
0	0	1	1	1	4
0	1	0	0	1	5
0	1	0	1	1	6
0	1	1	0	1	7
0	1	1	1	1	8
1	0	0	0	1	9
1	0	0	1	1	10
1	0	1	0	1	11
1	0	1	1	1	12
1	1	0	0	1	13
1	1	0	1	1	14
1	1	1	0	1	15
1	1	1	1	1	16

(b)

Figure 4.12: ADG1406 pin configuration and the corresponding truth table

For scanning method with various electrode configurations, every electrode from the array has to connect to the four possible outputs (two current electrodes and two voltage

electrodes) as discussed previously. That means a total of 400 electrode connections are needed to enable any random electrode selection on the array; the four connection lines for each electrode. Because of the system complexity and the PCB manufacturing limits, the system has been designed to perform only horizontal and vertical scan methods as shown in Figure 2.4 in Chapter 2.2.1. The horizontal and vertical selection of the four electrodes reduces the system complexity because any random two-dimensional electrode selection is not taken into account. However, this system still requires about 20 multiplexers to enable the automated measurement system. The detailed information is shown in Figure 4.13.

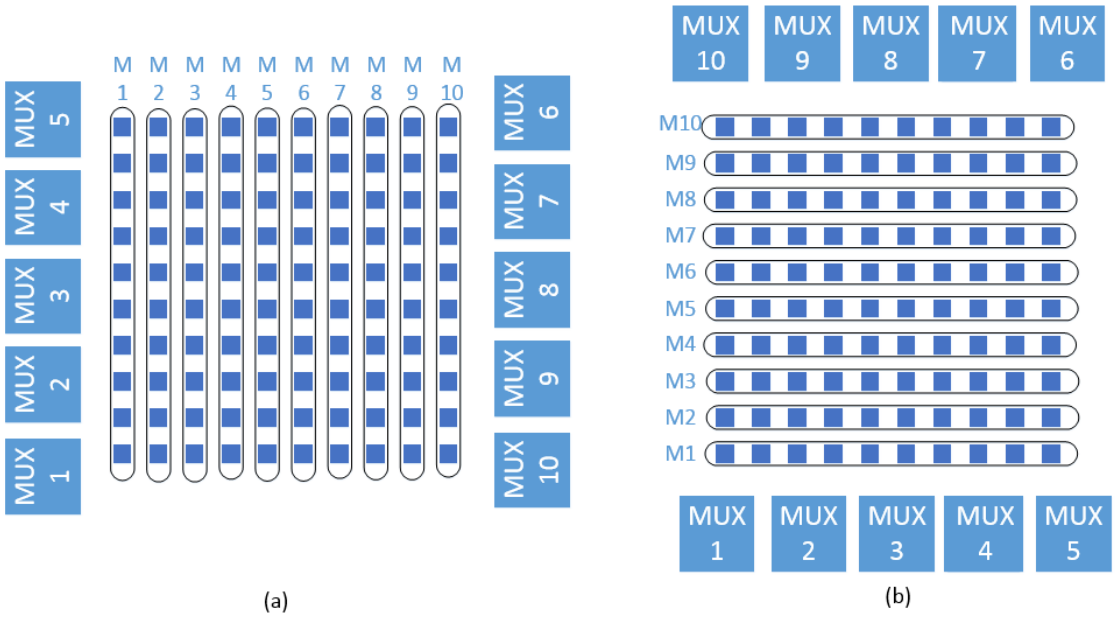

Figure 4.13: Multiplexer configurations for horizontal and vertical scanning mechanisms

Figure 4.13 (a) enables the horizontal scanning and (b) the vertical scanning of the electrode selections. In the 1-4-2-3 electrode selection case, a total of 7 measurements are performed to scan the one row. After the first row 7 measurements are taken, and then another 7 measurements are performed on the second row. 10 channels of each multiplexer

are connected to the 10 electrodes of each of the columns. As the measurement moves to next row, the binary addresses of the 10 multiplexers change correspondingly. In the same manner, 4 out of 10 multiplexers have to be selected whenever the measurement moves to next column. Thus, the other 4 multiplexers (Control Mux) are needed to switch the selected electrode sets to the current and voltage measurement circuits. The 10 channels of the Control Mux are connected to the output of 10 multiplexers whose channels are connected to the electrodes. Four outputs of the Control Mux then are connected to the current sourcing circuit and the voltage measurement circuit, respectively. For example, for the 3-4-5-6 electrode measurement in the first row, the Control Mux switched to the number 3, 4, 5, and 6 multiplexers. Then, 3, 4, 5 and 6 multiplexers are switched to channel zero to make a connection to first row. If the same 3-4-5-6 electrodes measurement is performed on the second or third row, the Control Mux still chooses the same 3-4-5-6 multiplexers, but 3, 4, 5 and 6 multiplexers are switched to channels one or two. This automatic electrode selection system is implemented with USB-1024LS, 24-channel digital I/O device from Measurement Computing by programming NI LabView 2013. USB-1024LS are comprehensive drivers for NI LabView and easy to program to generate a digital signal to control the binary bits of the multiplexers. All binary bits for control and electrode selection multiplexers are programmed by NI LabView. The NI LabView is a powerful tool for measurements and it is easy to use with its graphical interface.

CHAPTER 5

MEASUREMENT SETUP AND MEASUREMENT REUSLTS

5.1 Measurement Setup

The measurement process has been performed with a simple tissue boundary. The three-layer pork has been chosen as a test tissue because the muscle and fat layers should have different dielectric properties and is easily available.

The layout of the PCB was designed by PADS from Mentor Graphics. In compliance with the manufacturing specification, the minimum routing size is 6 mils (0.1mm) and the minimum drill size is 10 mils (0.254mm). Considering the minimum size of the thickness of the copper routing and the distance between these routings, the electrode size was set to 0.5 mm and the center-to-center distance between the electrodes was designed to be 3 mm. Figure 5.1 shows the PCB manufactured by Advanced Circuit.

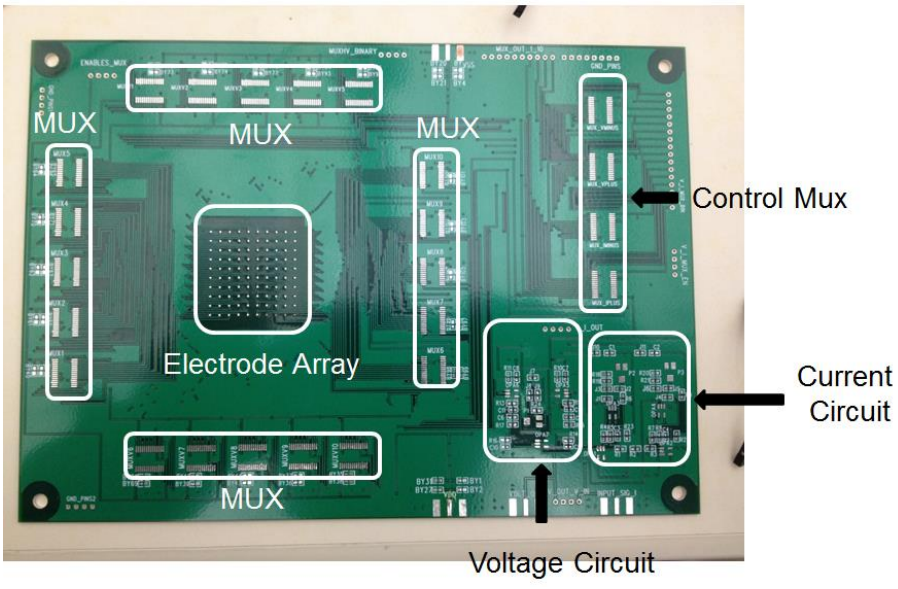

Figure 5.1: Printed circuit board manufactured by Advanced Circuit

First, the current and the voltage measurement circuit components were soldered onto the PCB and the performance was then tested. Figure 5.2 shows all components soldered for both circuits.

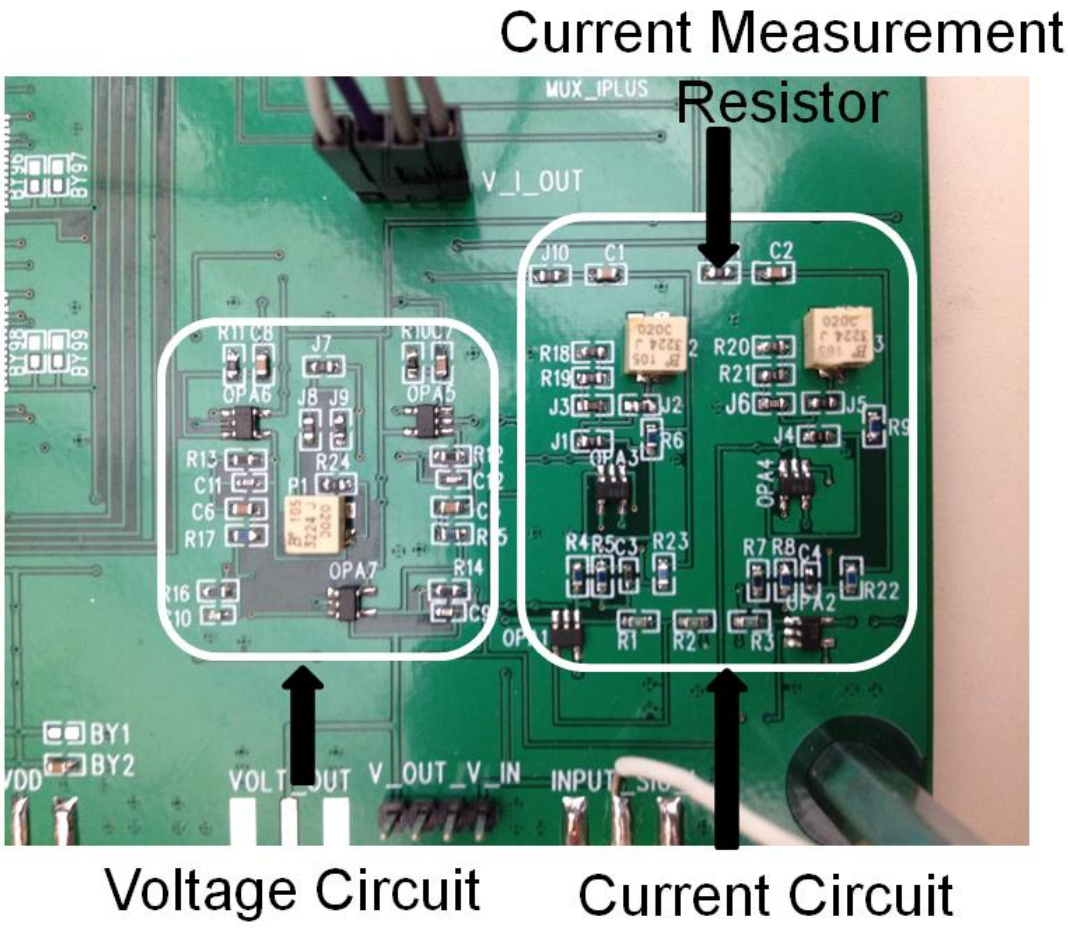

Figure 5.2: Fully constructed voltage and current circuits

Given the importance of the resistor matching mentioned in the TI Application note (2008), the modified Howland circuit was constructed using 0.05 % tolerance SMD resistors. OPA656 wideband, unity gain stable, FET-input operational amplifier from Texas Instruments has been used to design the current source circuit. For the instrumentation amplifier, the 1.6 GHz high gain bandwidth OPA657 operational amplifier has been used

from Texas Instruments as well. The key resistors that directly affect the output current and the gain of the instrumentation amplifier have been replaced with trimmers to provide flexibility in changing the current or the gain. 1MΩ 10% tolerance trimmer resistors from BOURNS have been used for both circuits.

Although the current value is known, because of the possible degradation of circuit performance in real implementation, the actual current is possibly different depending on the load condition. Since the test tissue impedance is unknown, the current has to be measured when the measurement is performed. To calculate the current, a resistor is soldered at the output of the current source. With the known resistor value and the measured voltage drop of the resistor, the actual current generated from the circuit can be measured. As shown in Figure 5.2, the 1 kΩ resistor was soldered at the output of the current circuit.

The current source circuit has been tested using various load conditions. The method was the same as in the simulation. A discrete resistor was connected at the output; the value was changed from 1k**Ω** ~ 10kΩ. The measured results are shown in Appendix A.

The current circuit was designed to generate a 100uA current. As shown in Table 2, a 100uA current was generated at 100 kHz, but the current changes little by little as the load varies. At 1 MHz, the current was not stable and the variation is large for different load conditions. This is because of possible stray capacitance at the output at high frequencies as Bertemes-Filho (2002) mentioned. At 1 kHz, the voltage signal is doubled and the current is also doubled. Overall, 100 kHz is chosen for the measurement frequency since it generates a relatively stable 100 uA current for various loads.

The instrumentation amplifier was also tested with the arbitrary signal generated from the current circuit.

After the two operating circuits, the multiplexer was soldered one by one and the switching performance was tested. Since the whole system was designed on one board, the testing and debugging process had to be done whenever new components were added. However, because of the complexity of the whole system and the difficulty of the debugging, the system was separated into two boards, which are the circuit portion and multiplexers.

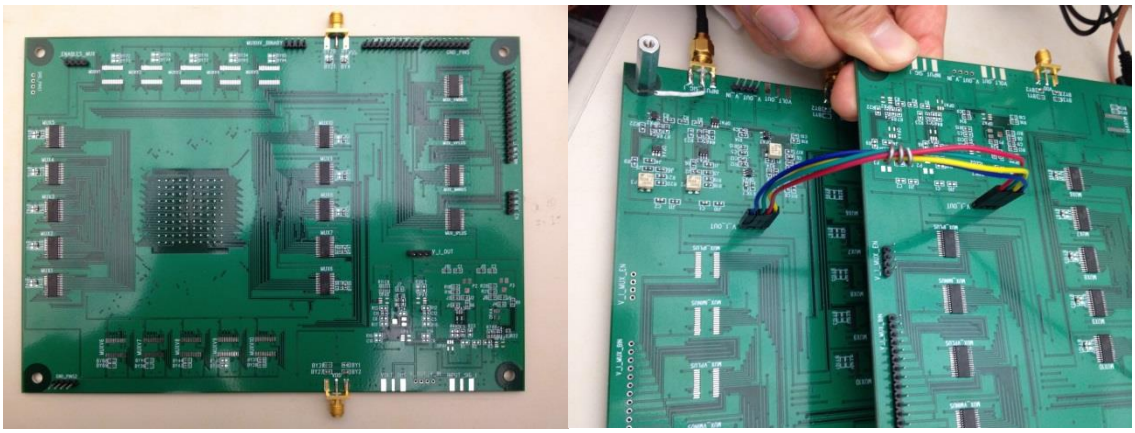

Figure 5.3: Multiplexer system and the circuits soldered on separate boards; only four current and voltage paths are connected

As shown in Figure 5.3, all multiplexers were soldered onto one board. The current and voltage measurement circuits were constructed into another board. Then, the final path of the current sourcing and voltage measurement electrodes are connected to the outputs of the current circuit and the inputs of the voltage measurement circuit as shown in Figure 5.3

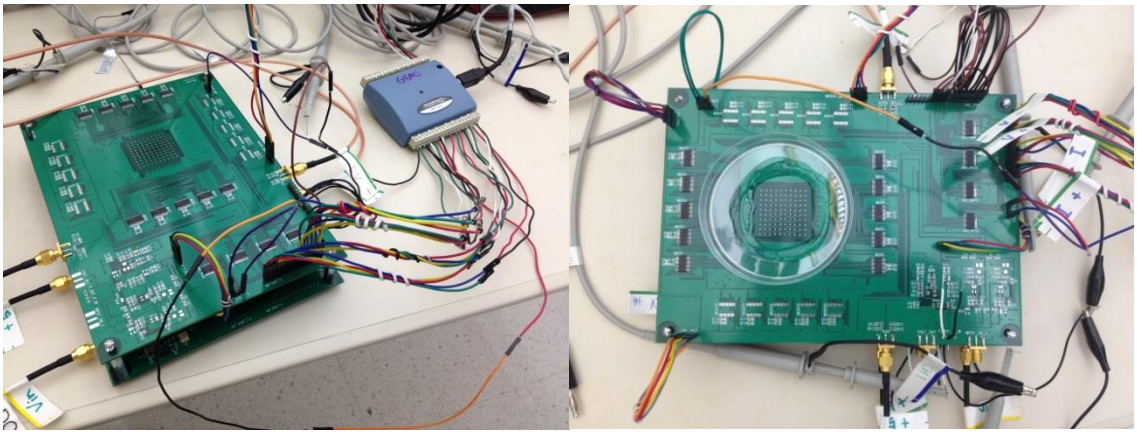

Figure 5.4: Complete PCB impedance sensor system with petri dish attached for tissue measurements

Figure 5.4 shows the complete impedance sensing system. A petri dish was attached to the electrode array with epoxy for the purposes of containing saline solution so to prevent the sample tissue from drying during the measurement process. The petri dish was provided by Mark P. Styczynski's lab in the School of Chemical & Biomolecular Engineering. A supply voltage of ±5 was supplied by the Agilent E3646A power supply, and the voltage signal was generated by the AFG3252 240 MHz Dual Channel arbitrary function generator from Tektronix. The current and voltage signal were measured by the MSO-X 2024A oscilloscope from Agilent Technologies. The oscilloscope is connected to the PC through the NI GPIB-USB-HS connector. The GPIB then enables NI LabView to control the oscilloscope, which can automatically store the data onto the PC. Figure 5.5 shows the whole measurement setup.

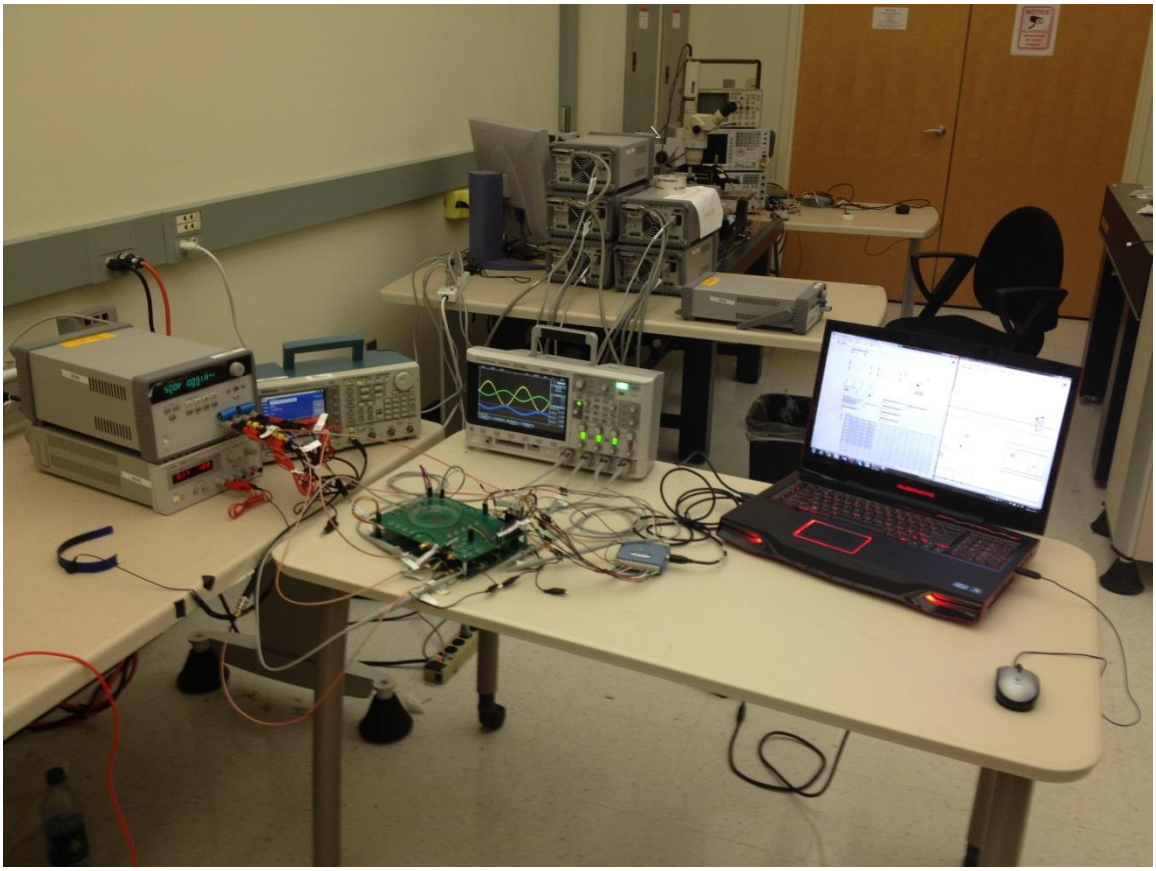

Figure 5.5: Experimental setup for the electrode array impedance sensor system for different tissue boundary detection

5.2 Measurement Results

Several different measurements were performed. First, the fat and the muscle of the three-layer pork were cut and the impedance measured. Then, the two-layer fat-muscle and the three-layer muscle-fat-muscle were put together to see the impedance mapping of the boundaries. In addition, the deep tissue penetration with large separated configuration has been performed to see whether the impedance mapping of different tissues can be generated through the layer. The sample tissues were cut into the proper size to fit onto the electrode

array on the board. Because of the complexity of the system, only the horizontal scanning measurement was performed. The tetrapolar impedance measurement was performed for the first four electrode set, and a total of 70 measurement data points were collected and reconstructed into an impedance mapping image by Matlab. Each measurement was stored into the NI LabView periodically and saved as an excel file after the last measurement. The potential voltage from the voltage electrodes was measured through the instrumentation amplifier. Then, the voltage drop of the resistor at the output of the current circuit was measured to calculate the actual current generated. Lastly, the phase difference between previous two values, the voltage from the tissue and the calculated current, was measured. Those measurement values were stored into the excel file and evaluated by Matlab.

Figures 5.7-5.12 show all the different measurement setups and the resulting impedance mapping image of the sample tissues. The same Matlab algorithm was used to generate the image as also done in the simulation. Figure 5.7 shows the measurement setup and the impedance mapping image of fat and muscle tissue, which are separately tested. As shown in the pictures, the muscle and fat were completely separated and cut to be the size of the electrode array. Muscle is typically considered a good conductor because it consists of many blood vessels through which the current can easily conduct. Thus, the muscle has a lower impedance value than the fat. The impedance mapping image in Figure 5.7 shows the high impedance distribution for the fat, and the lower impedance for the muscle. Although one type of tissue was measured, the impedance values varied all over the electrode array. However, the measurement error and the unexpected measurement point should be taken into account. Thus, the average impedance value and the impedance distribution tendency should be emphasized more in subsequent data analysis. The average

impedance distribution of the fat is about 280~300Ω and the average impedance of the muscle is 80~90Ω. Although the image shows a different color distribution, the actual impedance variation was not as different as the corresponding image may have portrayed.

After the first test, the two tissues were put together as shown in Figure 5.8. The measurement was performed with the tissue oriented in two different directions. The tissue boundary was vertically and horizontally oriented on the electrode by simply rotating the sample tissues. The picture shows the detailed information of the measurement. As shown in the impedance mapping image, both horizontal and vertical cases show a clear boundary detection. These measurement results exactly matches the simulation in that the different tissue boundaries can be mapped out and it clearly shows on the impedance mapping images.

The next measurement was performed with three-layer tissues as shown in Figure 5.9. The pure muscle-fat-muscle tissues were placed on the electrode array as illustrated in the pictures. The measurement was performed in the same manner as the two layer measurements; vertical and horizontal direction. However, compared to the clear mapping image of the two layers, the results of the vertically oriented sample did not show a clear boundary detection. On the other hand, the image of the horizontally oriented sample clearly shows the three layer boundary. The main reason comes from the measurement direction. For the vertical orientation case, the size of one layer is smaller than the length of four electrodes and the measurement direction is orthogonal to the boundary lines. Therefore, the current passes through both tissues during every measurement, which measures two different impedance values from the different tissue components unless each layer size is longer than the length of four electrodes. This makes the boundary detection

ambiguous as shown in the image results. However, in the horizontally oriented sample, the boundary line is parallel to the measurement direction, which results in a clearer mapping image as shown in Figure 5.9.

The next measurement is for deep tissue penetration. Figure 5.10 shows the detailed tissue sample. The deep tissue measurement uses the largely separated electrode selection to verify whether the tissue boundary can be delineated from the longer distance. As shown in Figure 5.10, the fat and tissues were stacked vertically; the bottom layer is a fat sample and the top layer is mixed fat-muscle tissue. The measurement was performed with the 1-4-2-3 configuration first. Other measurements for the 1-5-2-4 and the 1-6-2-5 configurations were sequentially processed. The impedance mapping image in Figure 5.10 (a) is the result for the 1-4-2-3 configuration. The fat-muscle boundary on the top layer is not detected and the impedance distribution over the surface shows similar results as only fat was present in measurement 1. The image (b) shows the 1-5-2-4 result. This image still does not show a clear boundary detection although part of the region shows a high impedance region. The 1-6-2-5 configuration produces the impedance image (c). Image (c) shows the two clear layers, which delineates the boundary line corresponding to the sample tissue boundary. Although the top of the image looks like two layers exist, the mixed impedance measurement at the edge of the electrode array should be taken into account in the analysis.

With the same tissue sample, only the muscle part was removed as shown in Figure 5.11. The situation is the same as before, but the muscle part is replaced with the saline solution in the petri dish. The results image shows that the top side of the resulting image shows the average impedance of the bottom fat layer and the saline solution. The bottom side shows

the overall impedance of the thick fat layer, which should have a higher impedance than the fat-solution average impedance. The impedance of the saline solution was measured and the impedance of the saline solution showed a similar impedance value as the muscle tissue.

The last measurement was to test how the impedance varies about the anisotropic characteristic of the tissues. Anisotropy implies that a material has different physical properties in different directions, as in the grain of wood. The muscle tissue has fiber as shown in the picture in Figure 5.12. The current conduction is easier when it flows along the along the muscle fiber but harder if the current flows orthogonal to the fiber. The graphical interpretation is shown in Figure 5.6 for better understanding.

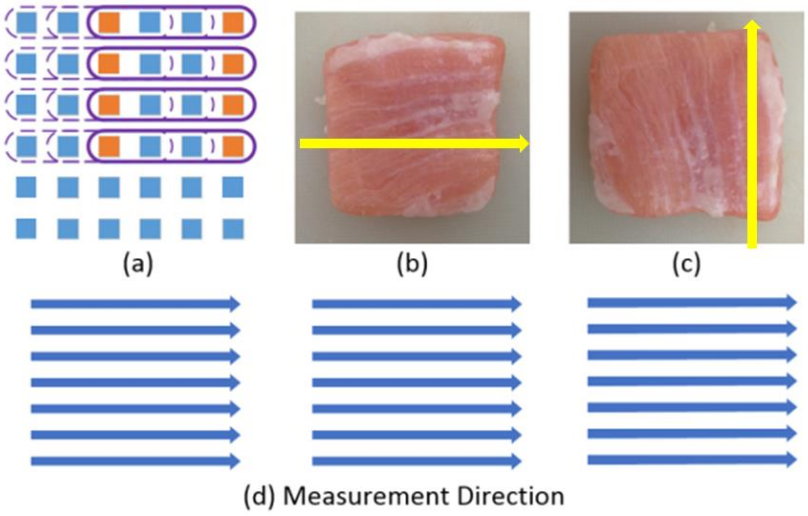

Figure 5.6: Measurement direction on the electrode array shown in (d) and muscle fiber direction indicated by yellow arrow.

The arrows in Figure 5.6 (a) indicate the measurement direction on the electrode array, which is corresponding to the direction of the current flow. The yellow arrows in Figure 5.6 (b) and (c) also describe the direction of muscle fiber.

The two measurements were performed such that the fiber of the muscle was placed along the horizontal measurement direction. The second measurement was performed with the sample rotated by 90 degrees as shown in Figure 5.12. The results image shows that the first measurement produces a lower impedance (average of 90~95). The second measurement shows a higher impedance (average of 110~120). This result verifies that the impedance varies depending on the anisotropic property of the tissue.

Based on all the measurement results, the PCB-level implementation successfully showed the impedance mapping image of different tissue boundaries. The measurement results clearly proved that the validity of the electrode array impedance mapping system works as a real implementation.

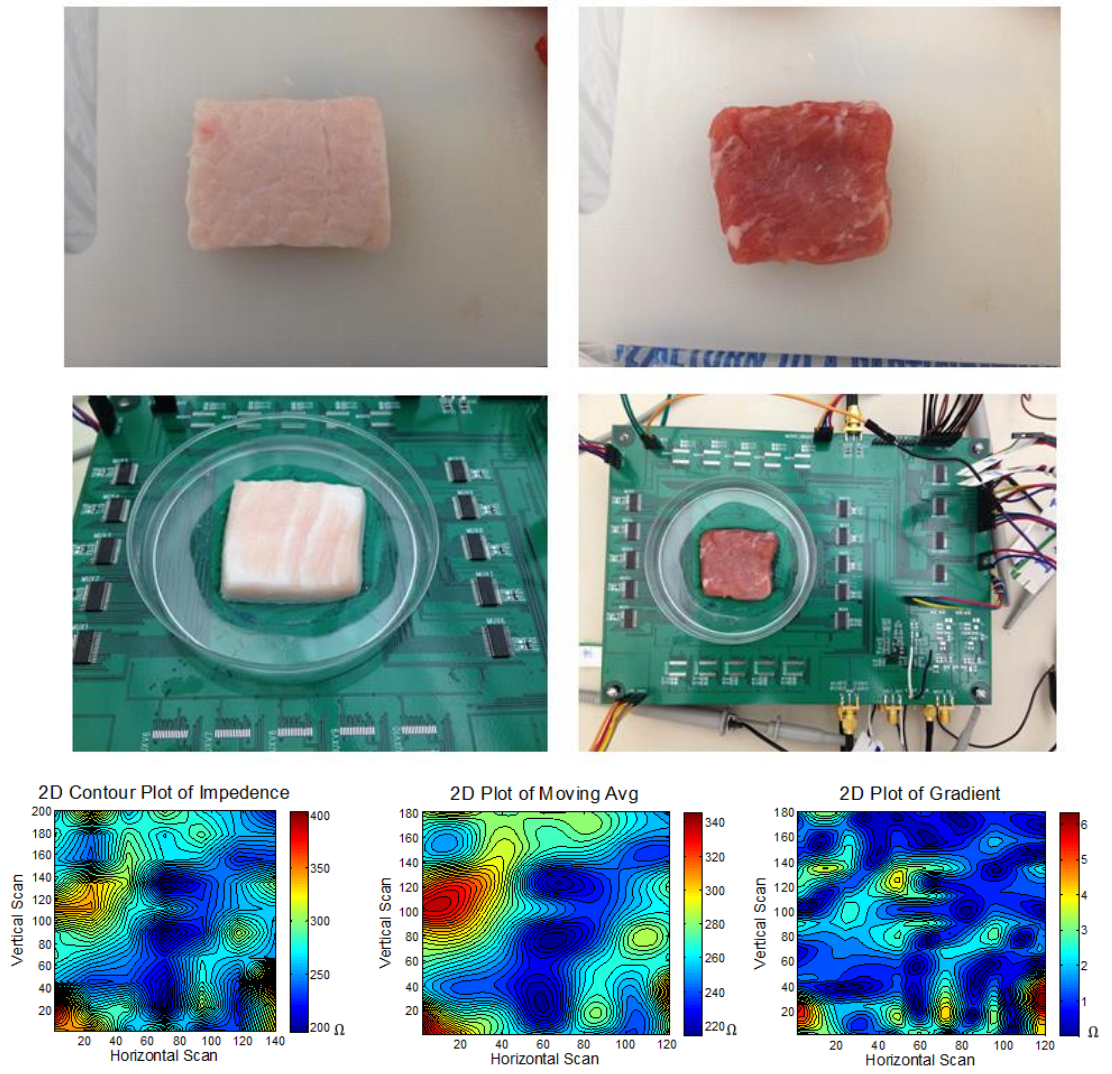

a. Impedance mapping image of the fat tissue of the pork
Configuration : [1-4-2-3]

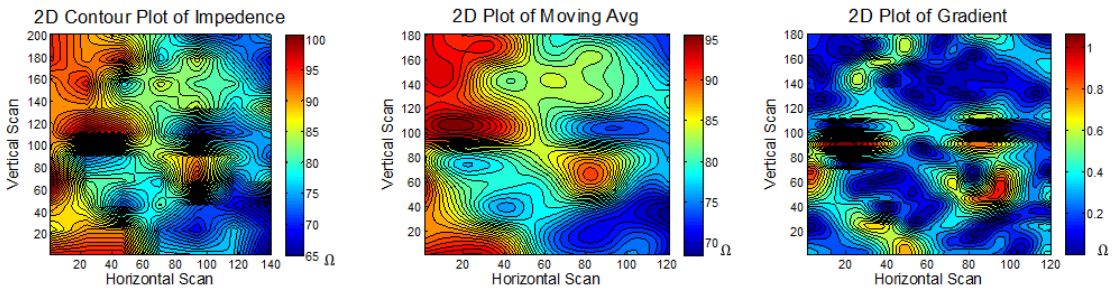

b. Impedance mapping image of the muscle tissue of the pork
Configuration : [1-4-2-3]

Figure 5.7: Measurement setup and impedance mapping image of fat and muscle tissues

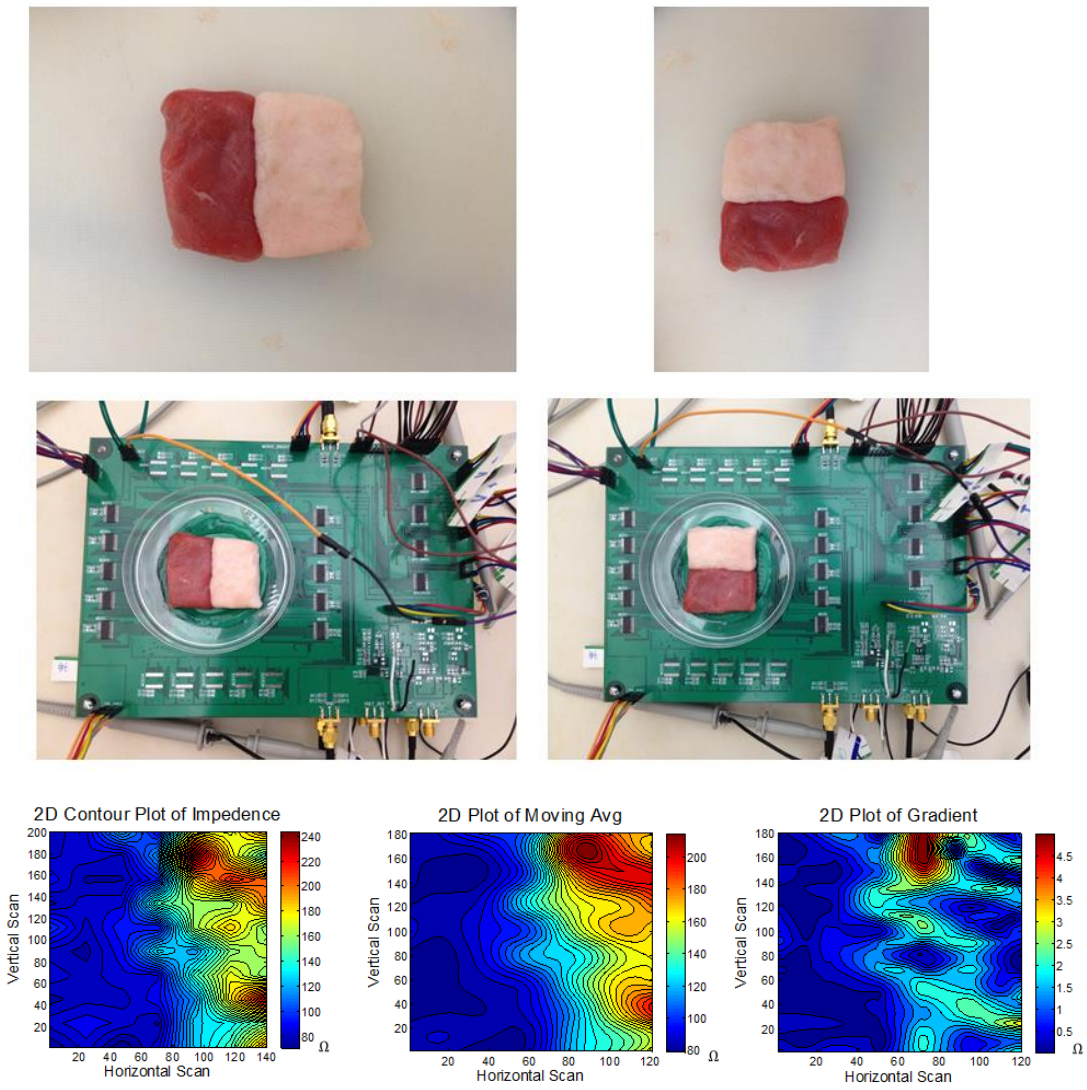

a. Impedance mapping image of the fat and muscle layers
Configuration : [1-4-2-3]

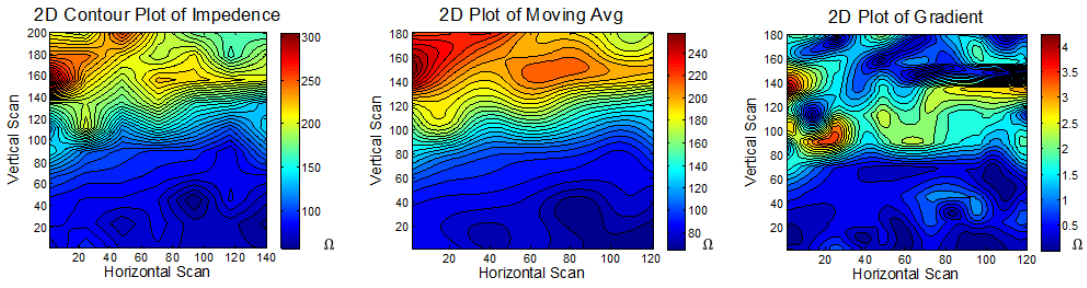

b. Impedance mapping image of the fat and muscle layers
Configuration : [1-4-2-3]

Figure 5.8: Measurement setup and impedance mapping image of two different layers

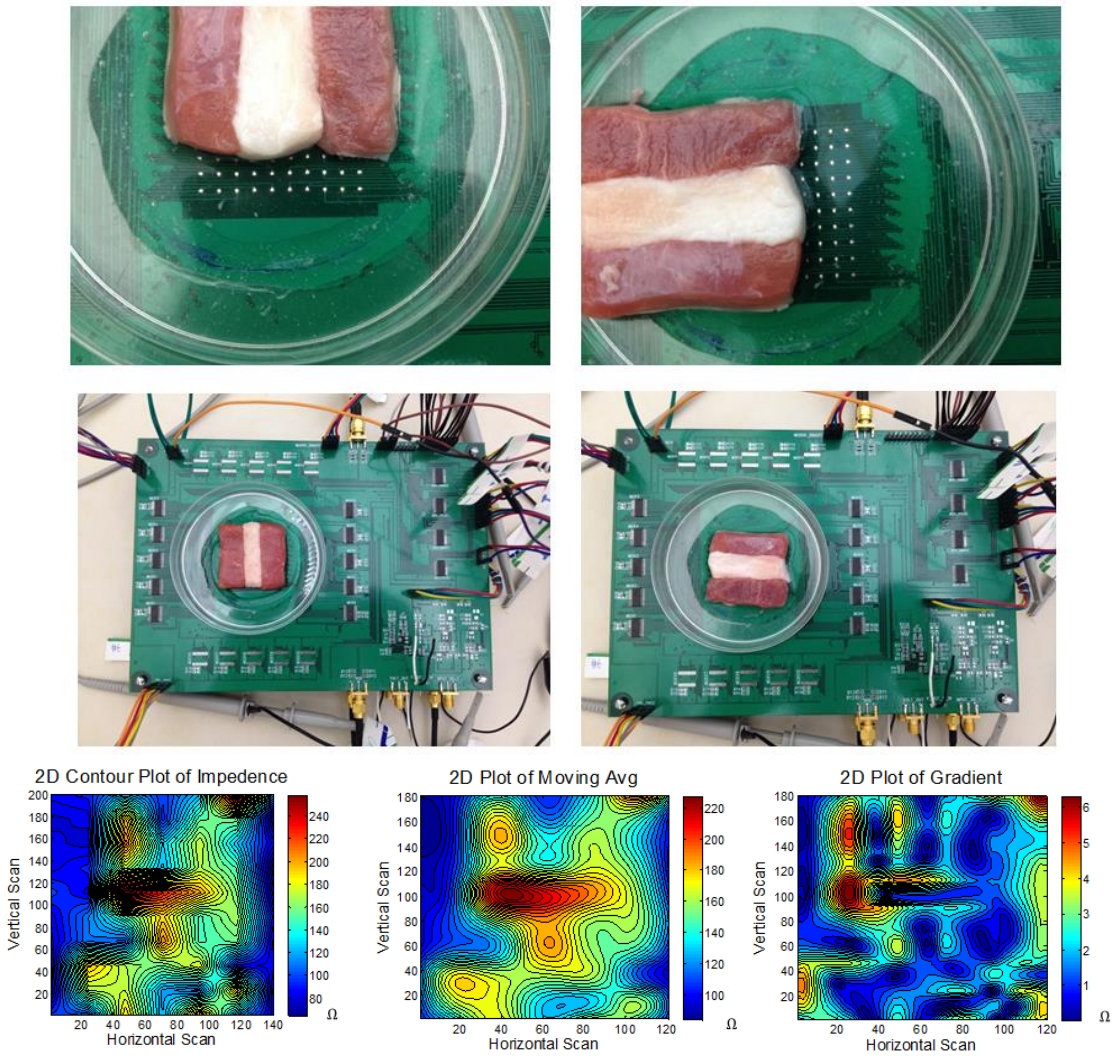

a. Impedance mapping image of the muscle-fat-muscle layers
Configuration : [1-4-2-3]

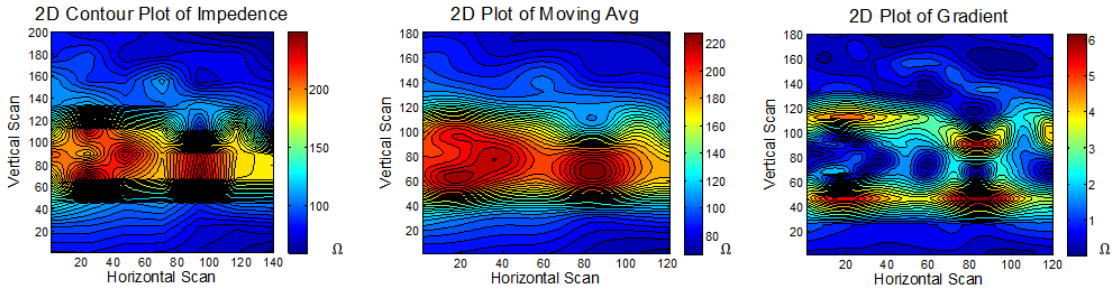

b. Impedance mapping image of the muscle-fat-muscle layers
Configuration : [1-4-2-3]

Figure 5.9: Measurement setup and impedance mapping image of muscle-fat-muscle three different layers

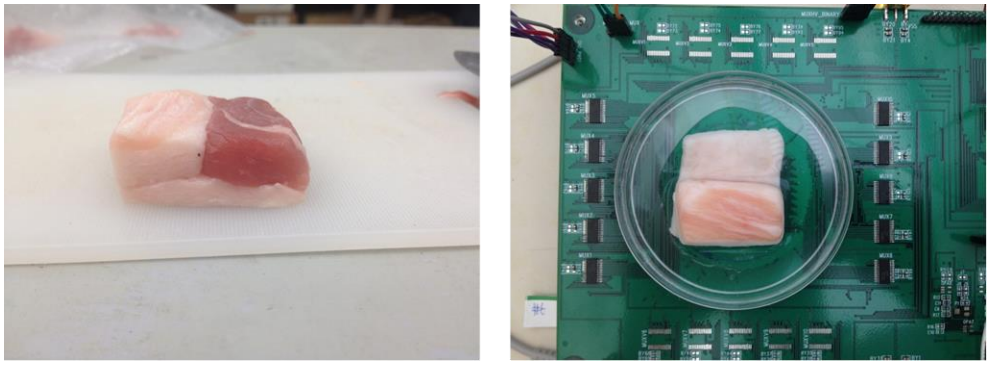

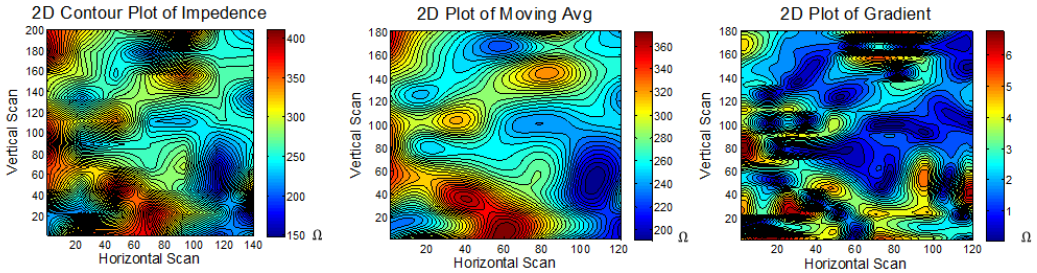

a. Impedance mapping image of the tissue penetration
Configuration : [1-4-2-3]

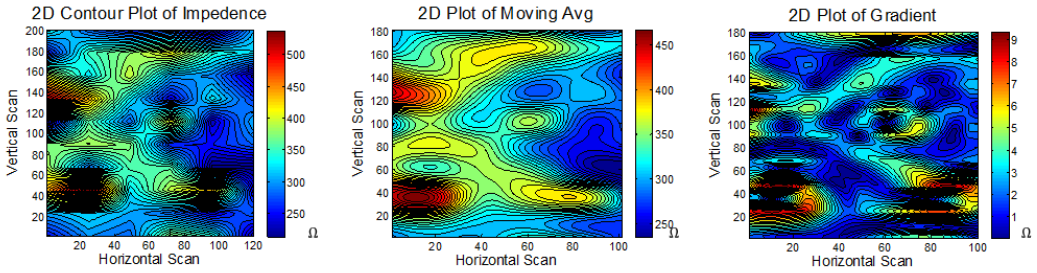

b. Impedance mapping image of the tissue penetration
Configuration : [1-5-2-4]

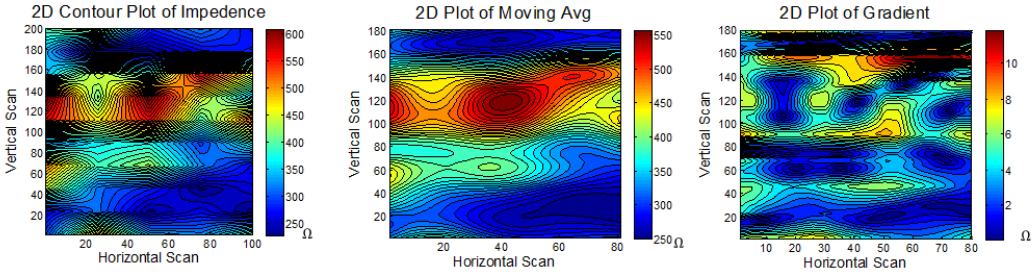

c. Impedance mapping image of the tissue penetration
Configuration : [1-6-2-5]

Figure 5.10: Measurement setup and impedance mapping image of the pile of tissues; fat layer at the bottom and mixed fat-muscle layer at the top

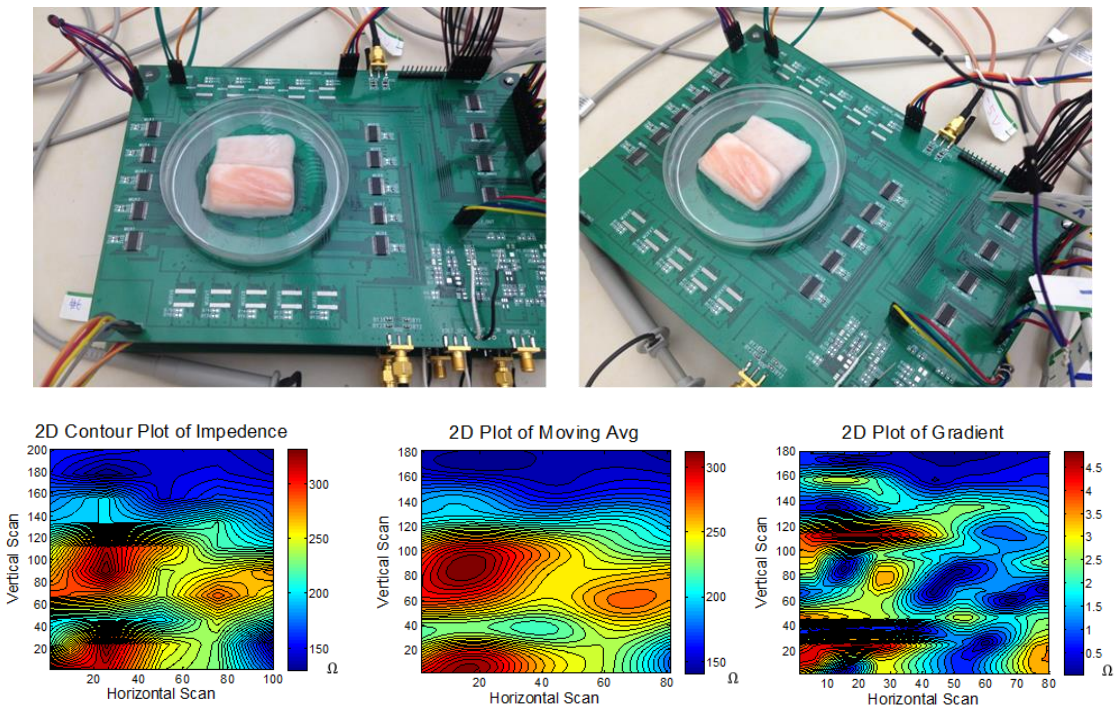

a. Impedance mapping image of the tissue penetration
Configuration : [1-6-2-5]

Figure 5.11: Measurement setup and resulting impedance mapping image of the pile of tissues; fat layer at the bottom and half side fat at the top

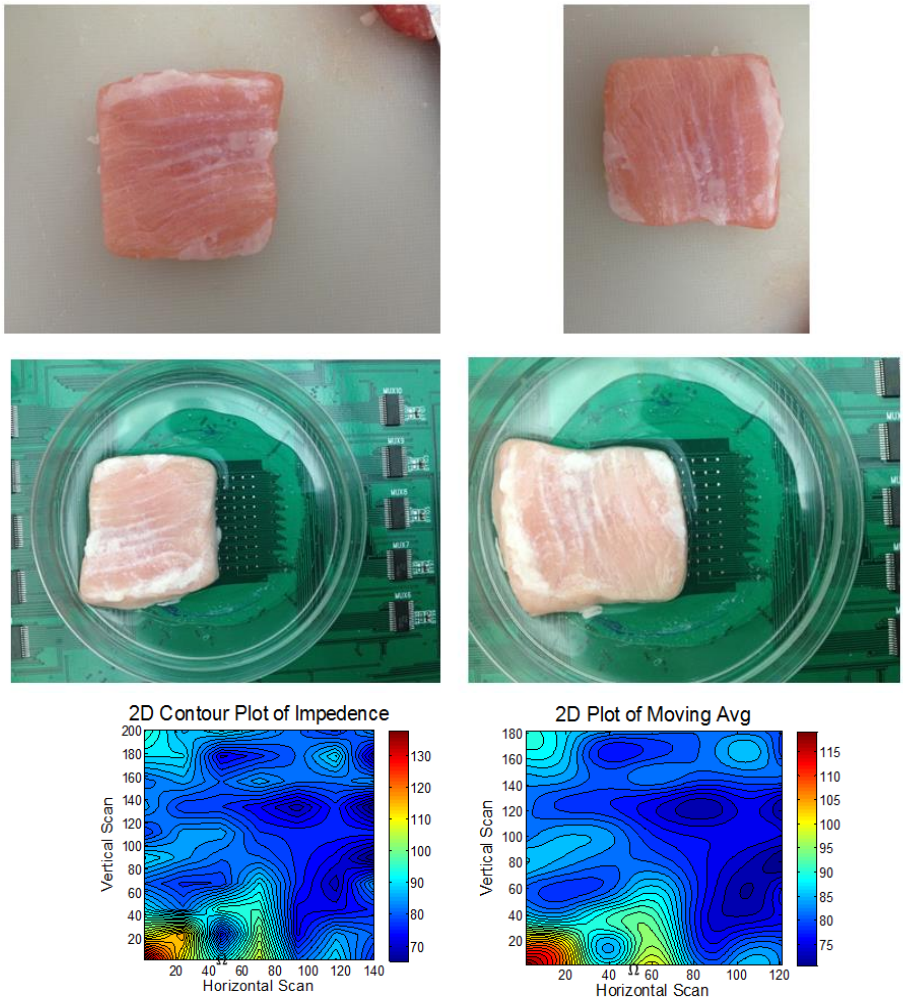

a. Impedance mapping image of the muscle Anisotropic test Configuration : [1-4-2-3]

b. Impedance mapping image of the muscle Anisotropic test Configuration : [1-4-2-3]

Figure 5.12: Measurement setup and impedance mapping image of testing impedance variation based on anisotropic property of the tissue

5.3 Discussion

The measurement results show that the PCB-level impedance mapping array sensor can delineate the boundary of two different tissues (muscle and fat). The simulation was focused on the brain tumor and how the tissue boundary is detected by the impedance array sensor. Although the experimental measurement sample was not an actual tumor tissue, both results can be correlated together in that the different tissue boundaries were able to be detected by the electrode array system and successfully reconstructed into impedance mapping images.

There were many unstable systematic problems exhibited that can possibly improve the system performance if addressed. First, the multiplexer system has too much routing and too many long lines which can cause significant degradation of the signal and increase noise. As discussed, the off-switch path current leakage of the multiplexers can be one of the major problems since the unknown current change would directly affect the voltage measurement of the tissue. Since the exact amount of leakage cannot be measured or estimated, off-isolation should be an important consideration when the multiplexer is selected. Also, the output resistor for measuring actual current should be placed right before the electrode array for more accurate measurements.

The stray capacitance of the PCB system can affect the output impedance of the current circuit and the input impedance of the voltage measurement circuit as well. Bertemes-Filho (2002) suggested using a negative impedance converter as a compensating circuit to improve the output impedance of the current circuit.

Accurate measurement is important, but also the correct data analysis is essential. As both the simulation and measurement results show, the impedance value is not always the same, even for the same tissues. There is always variation that may come from system tolerance, measurement conditions (temperature, humidity) or the tissue itself. In this thesis, Matlab was used to perform data analysis and plot the impedance mapping image. The Matlab contour function may not be accurate enough for an exact analysis of the impedance image as mentioned before. Further improved date processing is required for better visualizing and understanding of impedance mapping.

CHAPTER 6

SUMMARY AND CONCLUTSION

The bio-impedance measurement method has a lot of advantages in that it is simple, cheap, and can be designed as a portable device. The tetrapolar impedance measurement method has been widely used as a bioelectrical impedance measurement because it allows a more accurate impedance measurement by reducing contact impedance from the electrode surface. It has been verified that the different biological tissues have different dielectric properties and the impedance variation can therefore detect normal and malign tissues. In this thesis, the preliminary simulation proved that the electrode array system can detect different tissue boundaries (cylindrical and L shaped). A more realistic approach with MRI-derived brain/tumor models was performed and the results also successfully show the tumor boundary as impedance mapping images. As the real proof-of-concept demonstration, the PCB-level system was implemented and it produced the promising results by showing the muscle and fat tissue boundary detection in a 2D impedance mapping image.

The PCB system was implemented as a prototype for the real verification. The system can be further improved by solving issues presented in the discussion such as the current circuit output impedance problem, multiplexer off-path leakage and better PCB design with more flexibility. The thesis shows promising results and the design methodology can be directly leveraged to implement a fully integrated microscopic electrical impedance sensor array using commercially available Integrated Circuit (IC) technologies, such as Complementary Metal oxide Semiconductor (CMOS) process.

APPENDIX

Appendix A – Performance of the modified Howland Circuit

1kHz			100kHz			1 MHz		
Rload(Kohm)	Vpp Load	Current	Rload(Kohm)	Vpp Load	Current	Rload (Kohm)	Vpp Load	Current
0.56k	0.249 V	222 uA	0.56	0.121 V	108 uA	0.56	117 mV	104 uA
1k (0.99k)	0.41 V	207 uA	1 (0.99)	0.209 V	106 uA	1 (0.99)	0.193 V	97.5 uA
2k (1.97k)	800mV	203uA	2k (1.97k)	400 mV	102 uA	2k (1.97k)	332 mV	84.2 uA
3k (3.25k)	1.31 V	202 uA	3 (3.25)	0.61 V	94 uA	3 (3.25)	0.49 V	75 uA
4k (3.97k)	1.59 V	200 uA	4k (3.97k)	780 mV	98 uA	4k (3.97k)	530 mV	66.7 uA
5k (5.07k)	2.05 V	202 uA	5 (5.07)	0.96 V	95 uA	5 (5.07)	0.64 V	63 uA
8k (8.1k)	3.14 V	194 uA	8 (8.1)	1.41 V	87 uA	8 (8.1)	0.76 V	46.9 uA
10k (9.9k)	3.68 V	186 uA	10 (9.9)	1.66 V	82 uA	10 (9.9)	0.83 V	41.9 uA

REFERENCES

Bertemes-Filho, P. (2002), Tissue Characterization using an Impedance Spectroscopy Probe, Ph.D. thesis, University of Sheffield

Bertemes-Filho, P., Brown, B. H., & Wilson, A. J. (2000). A comparison of modified Howland circuits as current generators with current mirror type circuits.*Physiological Measurement*, *21*(1), 1.

Bertemes-Filho, P., Negri, L. H., Felipe, A., & Vincence, V. C. (2012). Mirrored Modified Howland Circuit for Bioimpedance Applicatios: Analytical Analysis, *First Latin-American Conference on Bioimpedance, Journal of Physics,* 407

Binette, J. S., Garon, M., Savard, P., McKee, M. D., & Buschmann, M. D. (2004). Tetrapolar measurement of electrical conductivity and thickness of articular cartilage. *Journal of biomechanical engineering*, *126*(4), 475-484.

Casas, O., Rosell, J., Bragós, R., Lozano, A., & Riu, P. J. (1996). A parallel broadband real-time system for electrical impedance tomography. *Physiological Measurement*, *17*(4A), A1.

Cherepenin, V. A., Karpov, A. Y., Korjenevsky, A. V., Kornienko, V. N., Kultiasov, Y. S., Ochapkin, M. B., ... & Meister, J. D. (2002). Three-dimensional EIT imaging of breast tissues: system design and clinical testing. *Medical Imaging, IEEE Transactions on*, *21*(6), 662-667.

Chaplin, M. "Water Structure and Science", http://www1.lsbu.ac.uk/water/ (Accessed March 5, 2013)

Foster, K. R. (2000), Dielectric Properties of Tissues, The Biomedical Engineering Handbook. Boca Raton: CRC Press LLC.

Fricke, H., & Morse, S. (1925). The electric resistance and capacity of blood for frequencies between 800 and 4½ million cycles. *The Journal of General Physiology*, *9*(2), 153.

Gabriel, C., Gabriel, S., & Corthout, E. (1996). The dielectric properties of biological tissues: I. Literature survey. *Physics in medicine and biology*, *41*(11), 2231.

Gabriel, S., Lau, R. W., & Gabriel, C. (1996). The dielectric properties of biological tissues: II. Measurements in the frequency range 10 Hz to 20 GHz.*Physics in medicine and biology*, *41*(11), 2251.

Gabriel, S., Lau, R. W., & Gabriel, C. (1996). The dielectric properties of biological tissues: III. Parametric models for the dielectric spectrum of tissues.*Physics in medicine and biology*, *41*(11), 2271.

Mishra, V., Bouyad, H., Schned, A., Hartov, A., Heaney, J., & Halter, R. J. (2012). A real-time electrical impedance sensing biopsy needle.

Ogunnika, O. T., Rutkove, S. B., Ma, H., Fogerson, P. M., Scharfstein, M., Cooper, R. C., & Dawson, J. L. (2010). A portable system for the assessment of neuromuscular diseases with electrical impedance myography. *Journal of medical engineering & technology*, *34*(7-8), 377-385.

Pethig, R. (1984). Dielectric properties of biological materials: Biophysical and medical applications. *Electrical Insulation, IEEE Transactions on*, (5), 453-474.

Pozar, D. M. (1998), Microwave Engineering, 4th ed., Wiley and sons, New York

Robillard, P. N., & Poussart, D. (1979). Spatial resolution of four electrode array.*Biomedical Engineering, IEEE Transactions on*, (8), 465-470.

Smith, J. G. (2008), Bioimpedance Mapping of the Cervix, Ph.D. thesis, Queensland University of Technology

Saulnier, G. J., Blue, R. S., Newell, J. C., Isaacson, D., & Edic, P. M. (2001). Electrical impedance tomography. *Signal Processing Magazine, IEEE*, *18*(6), 31-43.

Tidswell, T., Gibson, A., Bayford, R. H., & Holder, D. S. (2001). Three-dimensional electrical impedance tomography of human brain activity.*NeuroImage*, *13*(2), 283-294.

Thomas, K. (2005) Getting the most out of your instrumentation amplifier design. *Analog Applications Journal*, Texas Instrument.

Texas Instruments (2008) An-1515 A Comprehensive Study of the Howland Current Pump. Application report SNOA474A, January 2008

Voigt, T. (2011), Imaging Conductivity using Electric Properties Tomography – Initial Clinical Results in Glioma Patients, *General Assembly and Scientific Symposium*, 1-4

Wang, M., Yin, W., & Holliday, N. (2002). A highly adaptive electrical impedance sensing system for flow measurement. *Measurement Science and Technology*,*13*(12), 1884.

Wilson, B. (1981). A low-distortion bipolar feedback current amplifier technique.*Proceedings of the IEEE*, *69*(11), 1514-1515.

Yúfera, A., Rueda, A., Munoz, J. M., Doldán, R., Leger, G., & Rodriguez-Villegas, E. O. (2005). A tissue impedance measurement chip for myocardial ischemia detection. *Circuits and Systems I: Regular Papers, IEEE Transactions on*, *52*(12), 2620-2628.

Zhang, J., & Patterson, R. (2010). Non-invasive determination of absolute lung resistivity in adults using electrical impedance tomography. *Physiological measurement*, *31*(8), S45.